Article

Electric dipole moment drives the dynamics of the TNFR1 complex I signalosome

https://doi.org/10.1038/s41586-026-10304-1

Received: 28 September 2025

Accepted: 19 February 2026

Published online: 1 April 2026

Check for updates

Jianping Liu[1,4]✉, Jing Zhao[1,2,4], Jiayang Gao[1,2,4], Kun Zhao[1,2], Yaoyao Han[1,2], Jing Yang[1,3], Zefei Li[1,2], Jianyu Ye[1,2], Ziyu Sun[1,2], Fengyi Wang[1,2], Xinyi Liu[1,2], Zekai Li[1,2], Siyu Ji[1,2], Bo Liu[1], Cong Liu[1], Yixiao Zhang[1], Junying Yuan[1]✉ & James J. Chou[1,3]✉

Dynamic assembly of the complex I signalosome mediated by three death domain (DD)-containing proteins—TNFR1, TRADD and RIPK1—is key for transmitting extracellular TNF stimuli to intracellular NF-κB signalling in controlling 'live or die' cell fate[1]. This signalling hub features the rapid recruitment of TRADD and RIPK1 after engagement of TNFR1 by TNF for the formation of complex I, followed by timed disassembly for transition into downstream signalling complexes[2,3], but the mechanism driving the dynamic reversibility of complex I remains unclear. Here we captured the assembly core of complex I and determined its cryo-electron microscopy structure, showing a pentameric fibre comprising 31 DDs, with a single layer of a TRADD-DD pentamer sandwiched between multiple layers of TNFR1-DD and RIPK1-DD homopentamers. Structural analysis revealed a strong opposing electric dipole moment (EDM) generated by RIPK1-DD oligomerization relative to that of TNFR1-DD and TRADD-DD. Structure-guided mutagenesis in TNFR1–TRADD–RIPK1 pentameric fibres altering the EDM without affecting DD oligomerization demonstrated the role and mechanism of EDM in driving the dynamic reversibility mediating the rapid assembly and disassembly of complex I. Our study demonstrates a role for long-range interactions mediated by protein EDMs in driving the assembly and disassembly of super-signalling complex I for promoting NF-κB signalling.

TNF is a pivotal proinflammatory cytokine involved in a multitude of human diseases[4]. This is underscored by the considerable success of anti-TNF therapy in treating a wide range of inflammatory diseases[5]. TNFR1, the primary receptor of TNF, is highly expressed by cells of myeloid lineage, such as microglia and macrophages, which are the primary mediators of inflammation. Engagement of TNFR1 by extracellular TNF promotes the rapid formation of a transient intracellular signalosome, known as complex I. The core scaffold of complex I is formed by direct interaction of TNFR1 intracellular DD with two DD-containing proteins: the adaptor protein TRADD and the receptor-interacting protein kinase RIPK1[3,6–9]. In complex I, TRADD is critical for the recruitment of multiple ubiquitin ligases and ubiquitin modification proteins, including Lys63 ubiquitin ligases (TRAF2/5, cIAP1/2), the M1 ubiquitin ligase complex LUBAC, the editing enzyme A20 and ubiquitin-binding proteins like NEMO, leading to robust RIPK1 ubiquitination with Lys63 and Met1 chains that recruit TAK1 and IKK complexes for mediating pro-survival NF-κB signalling[10–13]. Complex I is a key signalling hub regulating the cell's live-or-die decision; its importance is manifested by diverse human inflammatory and neurodegenerative diseases associated with genetic mutations in the genes encoding the components of complex I[14]. However, the core architecture and principle that controls the dynamic formation and disassembly of complex I are unclear. It is also puzzling why and how complex I exhibits dynamic reversibility in its rapid disassembly shortly after its formation to promote NF-κB activation in the nucleus and, alternatively, release RIPK1 into the cytosol where it may form complex IIa with FADD and caspase-8 to promote apoptosis, or complex IIb with RIPK3 and MLKL to promote necroptosis[2,3]. Structural studies of TNF-triggered complex I have been impeded by the propensity of DDs to aggregate. In fact, all reported DD structures of TNFR1 or TRADD are either of mutants, or were determined under acidic conditions (pH of around 4–5) or with arginine-linked GlcNAcylation to block aggregation[15–17].

Here we investigated the structural principle governing the dynamic assembly and disassembly of TNF-induced complex I. We reveal that the core of complex I signalosome formed by wild-type (WT) TNFR1-DD, TRADD-DD and RIPK1-DD is a superhelical fibre in which a single layer of TRADD-DD pentamer is sandwiched between multilayer pentameric assemblies of TNFR1-DD and RIPK1-DD. Notably, EDMs of the three DDs (TNFR1-DD, TRADD-DD and RIPK1-DD) were found to be critical in driving the dynamic reversibility of complex I for promoting NF-κB signalling. Our study discovered a critical role of EDMs in reorganization and dynamics of super signalling complexes.

Assembly core of TNF-stimulated complex I

The engagement of TNF with TNFR1 initiates the rapid formation of the complex I signalosome where the interaction of intracellular TNFR1-DD

[1]Interdisciplinary Research Center on Biology and Chemistry, Shanghai Institute of Organic Chemistry, Chinese Academy of Sciences, Shanghai, China. [2]University of Chinese Academy of Sciences, Beijing, China. [3]State Key Laboratory of Chemical Biology, Chinese Academy of Sciences, Shanghai, China. [4]These authors contributed equally: Jianping Liu, Jing Zhao, Jiayang Gao. ✉e-mail: jpliu@sioc.ac.cn; junying_yuan@sioc.ac.cn; james_chou@mail.sioc.ac.cn

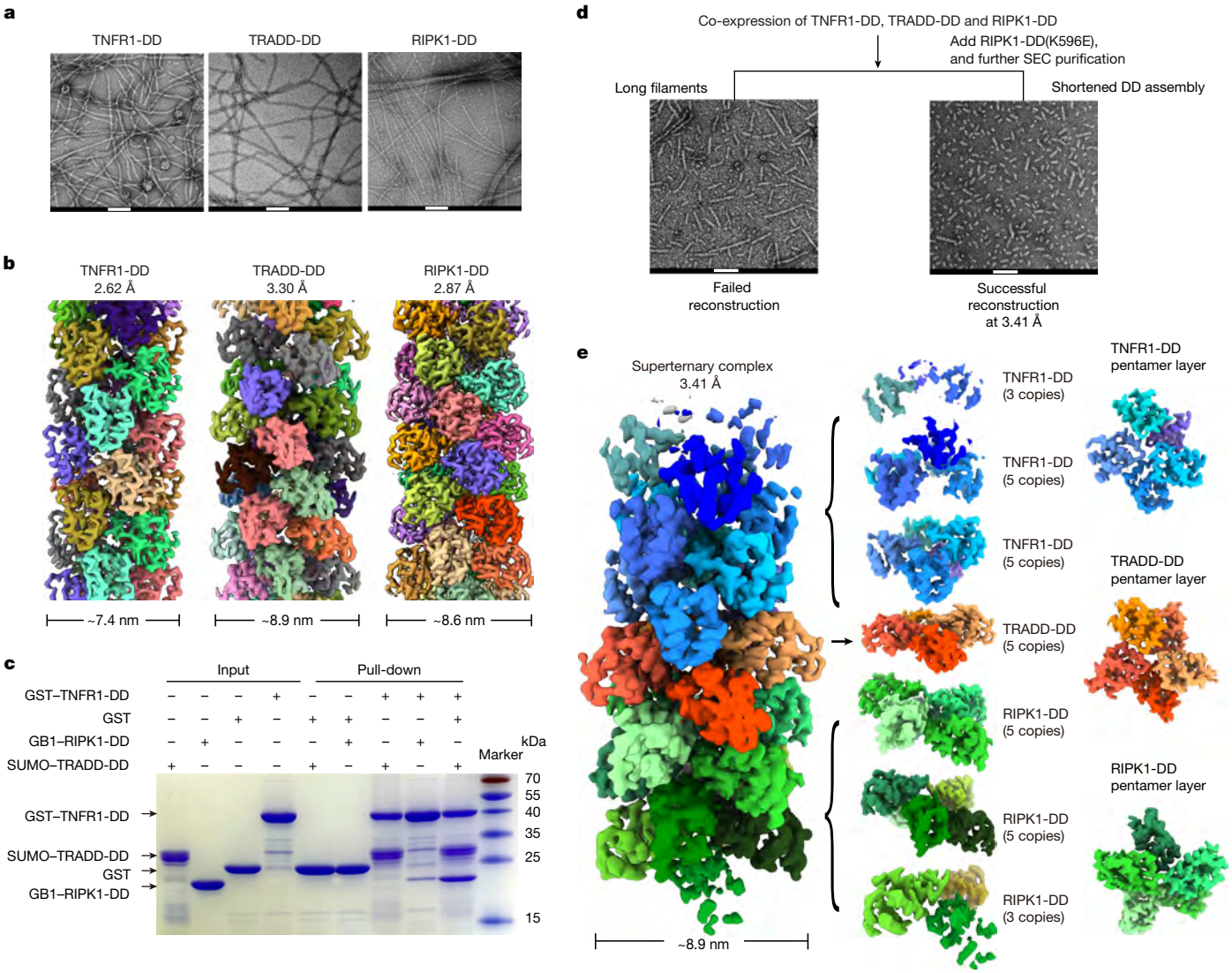


Fig. 1 | TNFR1-DD, TRADD-DD and RIPK1-DD assemble into a superternary complex. a, Negative-stain EM micrographs of three types of fibres formed by single type of TNFR1-DD, TRADD-DD or RIPK1-DD protein purified from *E. coli*. **b**, The cryo-EM structures of the three fibres in **a** were determined by helical reconstruction; the resolution and diameters are indicated. **c**, GST-pull-down assay showing the ability of GST–TNFR1-DD to recruit TRADD-DD as well as the requirement of TRADD-DD to further recruit RIPK1-DD. **d**, The strategy of using a RIPK1-DD mutant to modulate the ternary assembly of WT TNFR1-DD, TRADD-DD and RIPK1-DD. Negative-stain EM micrographs are shown of co-expressed WT TNFR1-DD, TRADD-DD and RIPK1-DD in the absence (left) and presence (right) of a RIPK1 mutant (K596E) that is defective for homo-oligomerization. SEC, size-exclusion chromatography. **e**, The cryo-EM structure of the superternary complex formed by WT TNFR1-DD, TRADD-DD and RIPK1-DD was determined at a resolution of 3.41 Å. The colour schemes of the DD subunits are as follows: blue, TNFR1-DD; orange, TRADD-DD; and green, RIPK1-DD. The ternary complex consists of 31 DD subunits or around 6 stacked DD pentamers. The results are representative of three independent experiments (**a**, **c** and **d**). Scale bars, 100 nm (**a** and **d**).

with TRADD-DD and RIPK1-DD constitutes the core of complex I to initiate the transmission of extracellular ligand binding to intracellular signalling[7,9,18]. We investigated the structural basis by which TNFR1-DD, TRADD-DD and RIPK1-DD interact to form the dynamic core that drives the formation and disassembly of complex I. Using negative-stain electron microscopy (EM), we found that WT human TNFR1-DD, TRADD-DD and RIPK1-DD proteins, when purified individually from *Escherichia coli*, all formed linear filaments with a diameter of around 10 nm (Fig. 1a). Consistently, all three types of DDs tagged with monomeric green fluorescent protein (mEGFP), when expressed individually in HeLa cells, also formed filaments (Extended Data Fig. 1a). We next determined the atomic structures of these filaments formed by a single type of TNFR1-DD, TRADD-DD or RIPK1-DD using the cryo-EM helical reconstruction method at a resolution of 2.6, 3.3 or 2.9 Å, respectively (Fig. 1b, Extended Data Fig. 1b,c and Extended Data Table 1). The outer surfaces of these filaments are highly charged with polarized distribution of charged residues (Extended Data Fig. 1d). The three types of DD filaments also show the same helical assembly pattern with a very similar helical rise and twist (Extended Data Fig. 1b,d).

We next examined interactions among the DDs of TNFR1, TRADD and RIPK1 that are important for complex I initiation. Pairwise GST pull-down assays showed that TNFR1-DD can directly bind to TRADD-DD and RIPK1-DD, but with substantially higher affinity to the former (Fig. 1c). The binding of RIPK1-DD to TNFR1-DD is considerably enhanced by the presence of TRADD-DD, consistent with the adaptor role of TRADD in recruiting RIPK1 to TNFR1[8] and suggesting the formation of a ternary complex when all three DD proteins are present (Fig. 1c). We successfully purified this ternary DD complex after co-expressing TNFR1-DD, TRADD-DD and RIPK1-DD in *E. coli* and found that they formed filaments with uniform diameters similar to the homotypic DD filaments (Fig. 1d). However, these filaments are shorter and adopt highly inhomogeneous length. Single-particle reconstruction

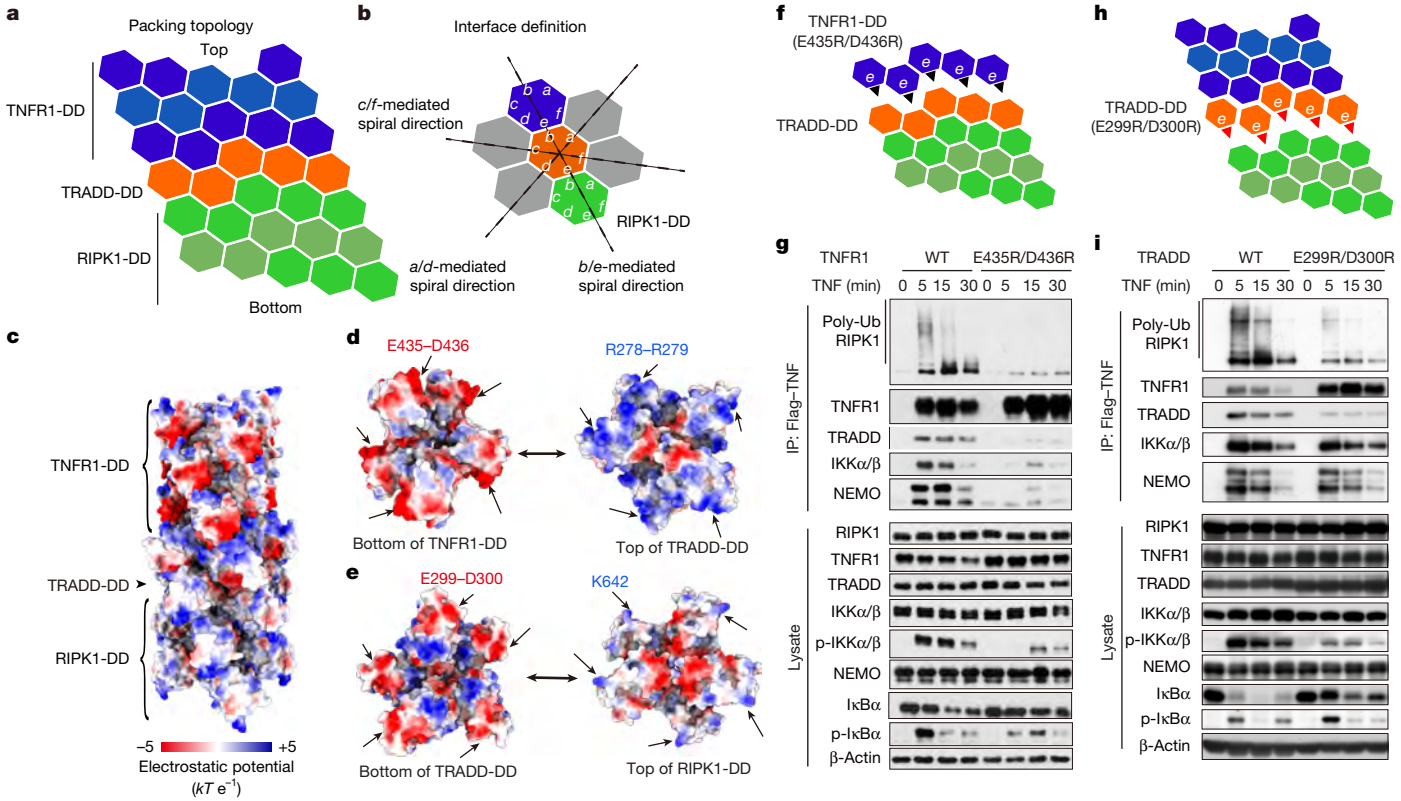


Fig. 2 | The structural basis for TRADD-DD pentamer as the adaptor for complex I formation. a, A schematic planar diagram of the packing topology of the TNFR1-DD–TRADD-DD–RIPK1-DD ternary complex. **b**, A diagram showing the definition of DD–DD packing interfaces and the directions of three types of spirals formed through three pairs of interfaces (*a*/*d*, *b*/*e* and *c*/*f*). **c**, Electrostatic potential surface revealing the highly charged surface of the DD super complex. **d**, Interlayer stacking interfaces showing the charge and shape complementation between the TRADD-DD and TNFR1-DD layers; the critical residues Glu435 and Asp436 in TNFR1 and Arg278 and Arg279 in TRADD are indicated by arrows. **e**, Interlayer stacking interfaces showing the charge and shape complementation between the TRADD-DD and RIPK1-DD layers; the critical residues Glu299 and Asp300 of TRADD and Lys642 of RIPK1 are indicated by arrows. **f**, Schematic of how the E435R/D436R double mutation in TNFR1 impairs its interlayer stacking with TRADD. **g**, Western blot analysis of TNF-induced (100 ng ml^{-1}) complex I and NF-κB activation in *TNFR1*-KO HeLa cells reconstituted with WT TNFR1 or TNFR1(E435R/D436R) mutant. **h**, Schematic of how the E299R/D300R double mutation in TRADD impairs its interlayer stacking with RIPK1. **i**, Western blot analysis of TNF-induced (100 ng ml^{-1}) complex I and NF-κB activation in *TRADD*-KO HeLa cells reconstituted with WT TRADD or the TRADD(E299R/D300R) mutant. The results are representative of three independent experiments (**g** and **i**).

of the longer filaments did not yield good resolution (Extended Data Fig. 2a), probably because the substantial variability in the layers of TNFR1-DD and RIPK1-DD prevented alignment and particle averaging.

To overcome this obstacle, we hypothesized that mixing the WT ternary filaments with a RIPK1-DD mutant partially defective for homotypic association with the WT RIPK1-DD may attenuate RIPK1-DD filament growth, therefore making the particles uniformly shorter for single-particle analysis. As such, we tested several mutations based on our RIPK1-DD filament structure and found that incubating the purified TNFR1-DD–TRADD-DD–RIPK1-DD complex with a small amount of RIPK1-DD(K596E) mutant generated homogeneous and shorter rod-like particles that could be analysed using cryo-EM (Fig. 1d and Extended Data Fig. 2b–f). Single-particle analysis of 68,501 rod-like particles determined a six-layer helical assembly structure at a resolution of 3.4 Å, comprising 2.5 layers of TNFR1-DD (13 copies), one layer of TRADD-DD (5 copies) and 2.5 layers of RIPK1-DD (13 copies) (Fig. 1e, Extended Data Fig. 2g,h and Extended Data Table 1). Furthermore, while the WT TNFR1-DD–TRADD-DD–RIPK1-DD assembly was spiked with the K596E RIPK1-DD mutant, SDS–PAGE analysis of the purified ternary complex showed no trace of the K596E mutant (Extended Data Fig. 2d). Thus, the RIPK1-DD(K596E) mutant was able to limit the growth of the ternary complex at the RIPK1 end through binding interference, but its own binding is not strong enough to be stably associated with the WT complex.

In the ternary complex, each DD occupies a quasi-equivalent position surrounded by six direct neighbours at six distinct interaction surfaces (Fig. 2a), designated *a*, *b*, *c*, *d*, *e* and *f* in Fig. 2b. These DD–DD interactions propagate to form a superhelical structure in which each layer of the helical structure consists of around five DDs (Fig. 2c). Interface pairs *a*–*d* and *c*–*f* are involved in both intralayer and interlayer DD–DD association (Fig. 2a,b). However, the interface pair *b*–*e* is involved in only interlayer DD–DD associations (Fig. 2a,b). These interactions are mediated mainly by salt bridges and hydrogen bonds between basic and acidic residues (Extended Data Fig. 3a-o). In particular, the layer–layer stacking among TNFR1-DD, TRADD-DD and RIPK1-DD exhibit strong electrostatic and shape complementation (Fig. 2d,e).

One of the interesting features of the six-layer ternary complex is that only one layer of pentameric TRADD-DDs is sandwiched between multiple layers of TNFR1-DD pentamers on top and RIPK1-DD pentamers at bottom. To rationalize this configuration, we computed the Gibbs free energy change (ΔG) for the interlayer association between DD layers using the program PRODIGY[19] based on our cryo-EM structures (Extended Data Fig. 3p). The ΔG values indicate that, among the homotypic associations between DD layers, the interlayer interaction of TNFR1-DDs is energetically most favourable ($\Delta G = -26.5$ kcal mol^{-1}), followed by that of RIPK1-DDs ($\Delta G = -24.7$ kcal mol^{-1}) and TRADD-DDs ($\Delta G = -23.3$ kcal mol^{-1}). However, the pentameric layer of TRADD-DDs exhibited a strong heterotypic association with the pentameric layers of

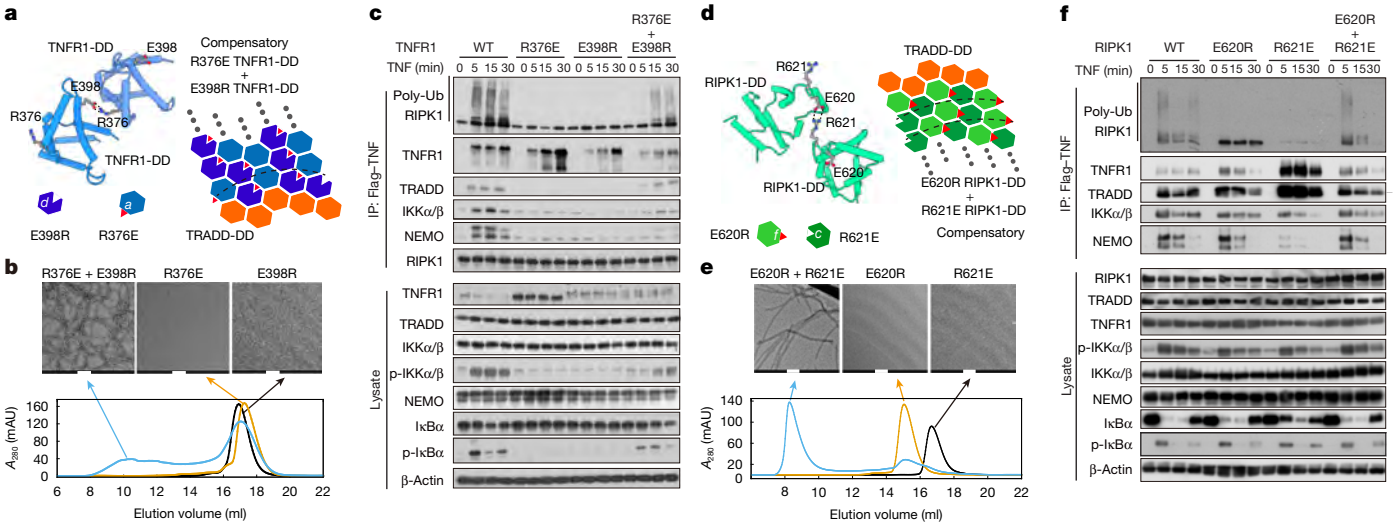


Fig. 3 | Homotypic oligomerization of TNFR1-DD and RIPK1-DD is critical for complex I signalling. a, Schematic of how a pair of charge-reversal mutants (R376E and E398R) of TNFR1 restore the association between interfaces *a* and *d* of TNFR1-DD. **b**, Negative-stain EM micrographs of individual, or a mixture of, TNFR1-DD(R376E) and TNFR1-DD(E398R) (top) and their corresponding size-exclusion chromatographs (bottom). For size-exclusion analysis, the R376E and E398R TNFR1-DDs contain the GB1 and SUMO tags, respectively, which were proteolytically removed for negative-stain EM analysis. **c**, Western blot analysis of complex I and NF-κB activation induced by TNF (100 ng ml^{-1}) stimulation in *TNFR1*-KO HeLa cells reconstituted by individual expression or co-expression of full-length R376E and E398R TNFR1 mutants. **d**, Schematic of how a pair of charge-reversal mutants (E620R and R621E) of RIPK1-DD restores the homo-association between interfaces *c* and *f* of RIPK1-DD. **e**, Negative-stain EM micrographs of individual, or a mixture of, E620R and R621E RIPK1-DD (top) and their corresponding size-exclusion chromatograms (bottom). For size-exclusion analysis, the E620R and R621E RIPK1-DDs contain the MBP and GB1 tags, respectively, which were proteolytically removed for negative-stain EM analysis. **f**, Western blot analysis of complex I and NF-κB activation induced by TNF (100 ng ml^{-1}) stimulation in *RIPK1*-KO HeLa cells reconstituted by individual expression or co-expression of E620R and R621E RIPK1 mutants. The results are representative of three independent experiments (**b**, **c**, **e** and **f**). Scale bars, 100 nm (**b** and **e**).

TNFR1-DDs (ΔG = −27.8 kcal mol^{-1}) and RIPK1-DDs (ΔG = −27.9 kcal mol^{-1}). Among the heterotypic interlayer interactions, the one between TNFR1-DDs and RIPK1-DDs is the weakest (ΔG = −22.5 kcal mol^{-1}). Thus, ΔG analyses of the different interlayer associations can provide the biophysical basis for a single layer of pentameric TRADD-DDs sandwiched between multi-layers of pentameric TNFR1-DDs on the top and RIPK1-DDs at the bottom and for TRADD to function as an adaptor in cellular TNFR1 signalling[18] (Extended Data Fig. 3p).

Adaptor function of TRADD in signalling

Interfaces *b* and *e* are responsible for interlayer association (Fig. 2a,b). Mutations on these interfaces would only affect interlayer contact of TRADD-DD with TNFR1-DD or RIPK1-DD, therefore offering an opportunity to unambiguously test the functional role of the single layer of TRADD in complex I. On interface *e* of TNFR1-DD, two negatively charged residues Glu435 and Asp436 associate with two positively charged residues Arg278 and Arg279 on interface *b* of TRADD-DD (Fig. 2d). Expression of a charge-reversal E435R/D436R TNFR1 mutant that disrupts the interlayer stacking between TNFR1-DD and TRADD-DD in *TNFR1*-knockout (KO) HeLa cells severely impaired the recruitment of TRADD, RIPK1, IKKα/β and NEMO, as well as ubiquitination of RIPK1 in complex I, which in turn reduced the phosphorylation of IKKα/β and phosphorylation and degradation of IκBα—the signal for mediating NF-κB activation (Fig. 2f,g). Similarly, *TRADD*-KO HeLa cells reconstituted with the TRADD(E299R/D300R) charge-reversal mutant, which disrupts its interface-*e*-mediated interlayer association with interface *b* of RIPK1-DD (Fig. 2h), also exhibited impaired recruitment of TRADD and RIPK1, phosphorylation of IKKα/β, and degradation of IκBα (Fig. 2i). Thus, the TRADD-DD layer between TNFR1-DD and RIPK1-DD layers is indispensable for complex I assembly and NF-κB signalling. These charge-reversal mutagenesis and energy calculations above demonstrate that a single layer of pentameric TRADD-DD functions as an adaptor through electrostatic complementation with TNFR1-DD and RIPK1-DD layers in complex I.

TNFR1 and RIPK1 DDs in complex I formation

In addition to the heterotypic DD–DD association that is essential for complex I formation, we next examined the function of homotypic TNFR1-DD and RIPK1-DD oligomerization in the superternary complex. On interfaces *a* and *d* of TNFR1-DD, a pair of conserved residues—Arg376 of *a* and E398 of *d*—form salt bridges between neighbouring TNFR1-DDs (Fig. 3a). We found that the purified R376E or E398R TNFR1-DD mutant alone was unable to form filament in vitro (Fig. 3b), whereas, notably, co-incubation of the R376E and E398R mutants restored the formation of filaments similar to that of the WT TNFR1-DD (Fig. 3b). In *TNFR1*-KO HeLa cells, mEGFP-tagged WT TNFR1-DD formed filaments, while the mEGFP-tagged TNFR1-DD(R376E) mutant or mCherry-tagged TNFR1-DD(E398R) mutant appeared mostly dispersed when expressed individually (Extended Data Fig. 4a). Consistently, co-expression of both mEGFP-tagged R376E and mCherry-tagged E398R mutants restored filament formation similar to that of the WT TNFR1-DD (Extended Data Fig. 4b). Consistent with the above observations, expression of individual full-length R376E or E398R TNFR1 mutants in *TNFR1*-KO HeLa cells was unable to support the formation of functional complex I (Fig. 3c), whereas co-expression of both the R376E and E398R mutants effectively restored complex I signalling (Fig. 3c). Furthermore, RNA-sequencing (RNA-seq) analysis revealed that TNF-mediated transcriptional response was significantly impaired in *TNFR1*-KO HeLa cells expressing either R376E or E398R TNFR1 mutant alone but was restored after co-expression of both (Extended Data Fig. 4c).

These observations indicate that the helical assembly of TNFR1-DD, which should accompany high-order receptor clustering on the plasma membrane, is critical for complex I formation. We therefore examined the consequence of TNFR1-DD oligomerization for TNFR1 clustering by tracking TNF-induced dynamic clustering of TNFR1 on the cell membrane using total internal reflection fluorescence (TIRF) microscopy. Using *TNFR1*-KO HeLa cells reconstituted with C-terminal mNeonGreen-tagged individual WT, R376E or E398R TNFR1, TIRF

Table 1 | Impact of interface mutations on recruitment of TRADD and RIPK1 to complex I and NF-κB signalling

Protein	TNFR1	TRADD		RIPK1					
Interface	*f*	*d*	*f*	*a*	*b*	*c*	*d*	*e*	*f*
Mutation	P368D	R235E	L261E	E626R	D618R	R621E	R603E	K596E	E620R
Impairs interlayer or intralayer	Both	Both	Both	Both	Interlayer	Both	Both	Interlayer	Both
TNFR1 recruitment	↑↑↑↑	↑↑↑↑	↑↑	↑↑	↑↑	↑↑	↑	↑	↑
TRADD recruitment	↓↓↓↓	↓↓↓	↓↓↓	↑↑	↑	↑↑	↑↑	↑↑	↑
RIPK1 recruitment and polyubiquitination	↓↓↓↓	↓↓↓	↓↓↓	↓↓↓↓	↓↓↓↓	↓↓↓	↓↓↓	↓↓↓	↓↓
NF-κB signalling	↓↓↓↓	↓↓↓	↓↓	↓↓	↓↓	↓↓↓	↓↓	↓↓	↓↓

A summary is shown for the increased/decreased levels of TNFR1, TRADD and RIPK1 recruitment to the complex I and RIPK1 ubiquitination in complex I in cells expressing the indicated TRADD mutant or RIPK1 mutant compared with that of cells expressing WT TRADD or WT RIPK1, indicated by up and down arrows, respectively. Raw data are presented in Fig. 3f and Extended Data Fig. 5a–g.

analysis showed that TNFR1 cluster formation stimulated by TNF in either of the single-mutant-expressing cells was severely impaired, while TNFR1 clustering was well restored by co-expression of both R376E and E398R mutants compared with cells reconstituted with WT TNFR1 (Extended Data Fig. 4d,e). This complementation assay suggests reciprocal enhancement between TNFR1 clustering on cell membrane and intracellular DD oligomerization.

Similar to TNFR1-DD, RIPK1-DD also forms multilayer of pentamers in the ternary DD complex (Fig. 1e). On interfaces *c* and *f* of RIPK1-DD, two conserved charged residues, Glu620 and Arg621, mediate associations between two neighbouring RIPK1-DDs (Fig. 3d). Either the E620R or R621E RIPK1-DD mutant purified from *E. coli* was unable to form filaments in vitro but, notably, co-incubation of the two mutants resulted in filaments similar to that of the WT RIPK1-DD (Fig. 3e). Consistently, in *RIPK1*-KO HeLa cells, individual expression of either mEGFP-tagged E620R or mCherry-tagged R621E RIPK1-DD mutant showed a dispersed distribution (Extended Data Fig. 4f), whereas co-expression of both formed filaments similarly to the WT RIPK1-DD (Extended Data Fig. 4g). Thus, the structural complementation between the E620R and R621E RIPK1-DD mutants offers a unique opportunity to examine the functional role of the RIPK1-DD helical assembly. In *RIPK1*-KO HeLa cells, expression of the E620R or R621E RIPK1 mutant impaired TNF-stimulated recruitment of RIPK1, IKKα/β and NEMO, as well as ubiquitination of RIPK1 in complex I (Fig. 3f). Consistently, co-expression of both E620R and R621E RIPK1 mutants corrected the levels of TNFR1 and TRADD in complex I comparable to that of the WT, and also restored all of the functional readouts (Fig. 3f). Furthermore, the RNA-seq data show that TNF-mediated transcriptional response was significantly impaired in *RIPK1*-KO HeLa cells expressing either E620R or R621E RIPK1, which was restored by co-expression of these two complementary RIPK1 mutants (Extended Data Fig. 4h). Thus, homotypic helical assembly of RIPK1-DD is also crucial for complex I signalling.

We also tested additional point mutations of the three DDs that impair both interlayer and/or intralayer interaction, and found that they all result in reduced recruitment of TRADD, RIPK1, IKKα/β and NEMO in complex I, accompanied with decreased polyubiquitination of RIPK1 and NF-κB signalling (Extended Data Fig. 5a–g). Notably, the stoichiometry of TNFR1 bound to TNF is consistently increased in the HeLa cells reconstituted with these complex I disruptive mutants including TRADD R235E and L261E, as well as RIPK1 K596E, R603E, E626R, D618R, E620R and R621E (Table 1, Fig. 3f and Extended Data Fig. 5b–g). Furthermore, co-expression of complementary mutants such as RIPK1(E620R) and RIPK1(R621E), which restored the intracellular helical filament formation, also restored the levels of TNF-engaged TNFR1 on the cell membrane comparable to that of the WT (Fig. 3f). These results suggest a restrictive impact of the intracellular superhelical assembly of TNFR1-DD–TRADD-DD–RIPK1-DD on the engagement of the TNFR1 extracellular domain (ECD) with ligand TNF.

Stoichiometry of TNFR1-DD in complex I

Another interesting feature of the superternary structure is approximately 2.5 layers of TNFR1-DD pentamer. This was unexpected as it is structurally possible for just one layer of TNFR1-DD to recruit a layer of TRADD-DD. We therefore investigated the minimum number of TNFR1-DD domains capable of supporting the formation of complex I. This question can be addressed by examining the geometrical compatibility between receptor clustering at the extracellular and intracellular levels. The intracellular linker (residues 233–354) of TNFR1 connecting the transmembrane domain (TMD) to the DD is predicted by AlphaFold as a flexible loop, which physically restricts the number of DDs that can be assembled away from the membrane and TMD. We tested the effect of shortening this linker on complex I assembly by generating a series of TNFR1 mutants with deletions of the intracellular loop (Fig. 4a). *TNFR1*-KO HeLa cells reconstituted with the TNFR1(Δ245–354) mutant, which retained only 12 residues between TMD and DD, did not support complex I formation after TNF stimulation (Fig. 4b). Notably, extension of the linker to 17 or 25 residues completely restored complex I formation, even to a higher level than that of the WT TNFR1 (Fig. 4c). These data indicate that the linker length of TNFR1 is crucial for TNFR1 signal transduction.

We next built models for the core of TNFR1 complex I on membrane by combining our superternary structure with the cryo-EM structure of multimer-of-trimer TNFR1-ECD–TNF (in trigonal planar arrangement)[20] and the NMR structure of the TNFR1-TMD trimer[21]. Modelling showed that a 12-residue linker between the TMD and DD is long enough for the assembly of only a single layer of TNFR1-DD pentamer beneath the plasma membrane (Fig. 4d), while a 17-residue linker is long enough for assembling around 2.5 layers of TNFR1-DD pentamers (Fig. 4e). The sharp transitions in the DD layer number and the ability to support complex I formation between the two deletion mutants, namely TNFR1(Δ245–354) and TNFR1(Δ250–354), strongly suggest that the 2.5 layers of TNFR1-DD pentamer observed in our cryo-EM structure is functionally meaningful and required for recruiting TRADD to initiate complex I formation. Similar modelling suggests that expanding the extracellular cluster beyond tetramer-of-trimer would result in TNFR1-ECD of the most peripheral trimer rotating away from the TMD by at least 13 nm, which cannot be accommodated by the ECD–TMD linker (around 10 nm) unless the membrane is severely deformed (Extended Data Fig. 6).

Function of EDM in dynamic DD helical assembly

We noted that a pronounced feature of the helical oligomers of TNFR1-DD, TRADD-DD and RIPK1-DD is the highly polarized distribution of positively and negatively charged residues on the surface which can lead to strong EDMs (Fig. 5a). We performed EDM calculations on the ternary complex[22] and found that the EDMs of TNFR1-DD and TRADD-DD pentamer layers are oriented 2.4° and 11.0°, respectively,

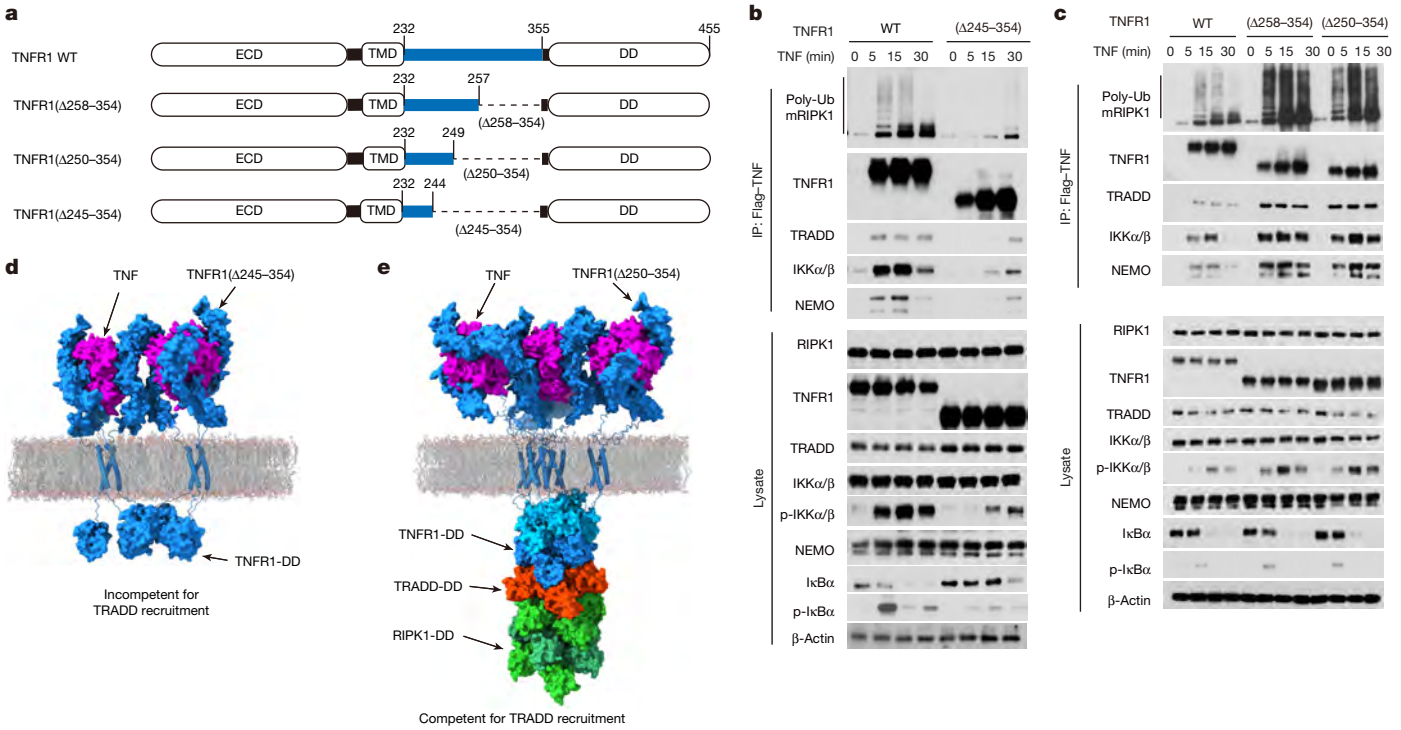


Fig. 4 | Homotypic stoichiometry of TNFR1-DD in receptor clustering and complex I formation. a, Illustration of TNFR1 mutants with a serial loop deletion between the TMD and DD. **b**, Western blot analysis of complex I formation and NF-κB activation induced by TNF (100 ng ml^{-1}) in *TNFR1*-KO HeLa cells reconstituted with WT TNFR1 or TNFR1(Δ245–354) mutant. **c**, Western blot analysis of complex I formation and NF-κB activation induced by TNF (100 ng ml^{-1}) in *TNFR1*-KO HeLa cells reconstituted with WT TNFR1, TNFR1(Δ258–354) or TNFR1(Δ250–354) mutant. **d**, A structural model showing that a 12-residue linker between TMD and DD in TNFR1(Δ245–354) is sufficient for only one layer of TNFR1-DD pentamer formation, which is incompetent for recruiting TRADD-DD and RIPK1-DD. **e**, A structure model showing that a 17-residue linker between the TMD and DD in TNFR1(Δ250–354) is long enough for stacking of about two layers of TNFR1-DD pentamers, which is competent for recruiting TRADD-DD and RIPK1-DD for complex I formation. The results are representative of three independent experiments (**b** and **c**).

relative to the helical axis of the ternary complex (*z*), whereas the EDM of RIPK1-DD layers are pointing almost in the opposite direction, 174.9° away from the *z* axis. Thus, the dipole–dipole interactions between the TNFR1-DD and TRADD-DD layers are attractive and energetically favourable, enabling the rapid recruitment of TRADD to oligomerized TNFR1. By contrast, the EDMs from the RIPK1-DDs exert repulsion between the RIPK1-DD and TRADD-DD/TNFR1-DD layers, suggesting that the growth of the RIPK1-DD filament would gradually build up EDM repulsion and ultimately cause RIPK1-DD dissociation from complex I (Fig. 5b). Thus, the repetitive arrangement of RIPK1-DD units in the ternary DD complex can build up a substantial EDM repulsion along the helical axis, proportional to the length of the filament, which may contribute to the instability of the complex.

This hypothesis predicts that mutations in RIPK1-DD that only reduce the cumulative EDM of RIPK1-DD layers and do not alter the DD–DD binding surfaces would effectively increase the amount and lifetime of RIPK1 in complex I; conversely, increasing the EDM of RIPK1-DD layers would reduce RIPK1 in complex I. To test this hypothesis, we introduced charge residue substitution at 3 sites (Thr579, Thr580 and Thr583) on the periphery of RIPK1-DD filaments that are not involved in the DD–DD binding (Extended Data Fig. 7a). Negative-stain EM showed that the purified triple-point T579D/T580D/T583D (3D) and T579R/T580R/T583R (3R) RIPK1-DD mutants form filaments that are indistinguishable from the WT RIPK1-DD filaments according to Fourier-transformed power spectrum of averaged two-dimensional cryo-EM images (Extended Data Fig. 7b,c). Moreover, the mEGFP-tagged 3R, 2D or 3D RIPK1-DD mutant also oligomerizes in *RIPK1*-KO HeLa cells similarly to the WT RIPK1-DD (Extended Data Fig. 7d). Mutation of Thr579, Thr580 or Thr583 to Asp or Arg increases or decreases the EDM of the RIPK1-DD pentamer, approximately in proportion to the number of Asp or Arg residues (Fig. 5c). Thus, these EDM-modulating mutations offer an opportunity to test the impact of EDM on complex I assembly.

In the *RIPK1*-KO HeLa cells reconstituted with either WT or single, double or triple T-to-D (or T-to-R) RIPK1 mutants, immunoprecipitation of complex I showed that the single mutation T583R, which decreases the EDM of RIPK1-DD pentamer from 1,245 to 1,126 Debye (Fig. 5c), doubled the recruitment of RIPK1 to complex I compared to WT (Fig. 5d). By contrast, the single mutation T583D that increased the EDM to 1,449 Debye decreased the amount of RIPK1 by around 30% (Fig. 5e). Additional mutations of Thr579 and Thr580 to Arg and Asp further increased and decreased, respectively, the recruitment of RIPK1, IKKα/β and NEMO in complex I (Fig. 5d,e). The plot of the RIPK1 levels in complex I after 5-min TNF stimulation of *RIPK1*-KO HeLa cells expressing WT RIPK1 or 6 RIPK1 mutants shows a strong negative correlation between the EDM of RIPK1-DD pentamer and the amount of RIPK1 in complex I (Fig. 5c).

We next investigated the functional impact of the RIPK1-DD EDM on NF-κB signalling. Analysis using quantitative PCR with reverse transcription (RT–qPCR) revealed that, when stimulated by different levels of TNF (1, 10, or 100 ng ml^{-1}), *RIPK1*-KO HeLa cells reconstituted with the 3R and 3D mutants consistently increased and decreased, respectively, the expression of *A20* (a well-established NF-κB-target gene) compared with cells reconstituted with WT RIPK1 (Extended Data Fig. 7e–g). The effect of EDM was also substantiated by RNA-seq analysis. The expression of the 3R and 3D mutants in *RIPK1*-KO HeLa cells enhanced and depressed, respectively, TNF-stimulated gene expression compared with the WT (Extended Data Fig. 7h). These results suggest a substantial role of EDMs in regulating the dynamic formation of complex I and NF-κB signalling.

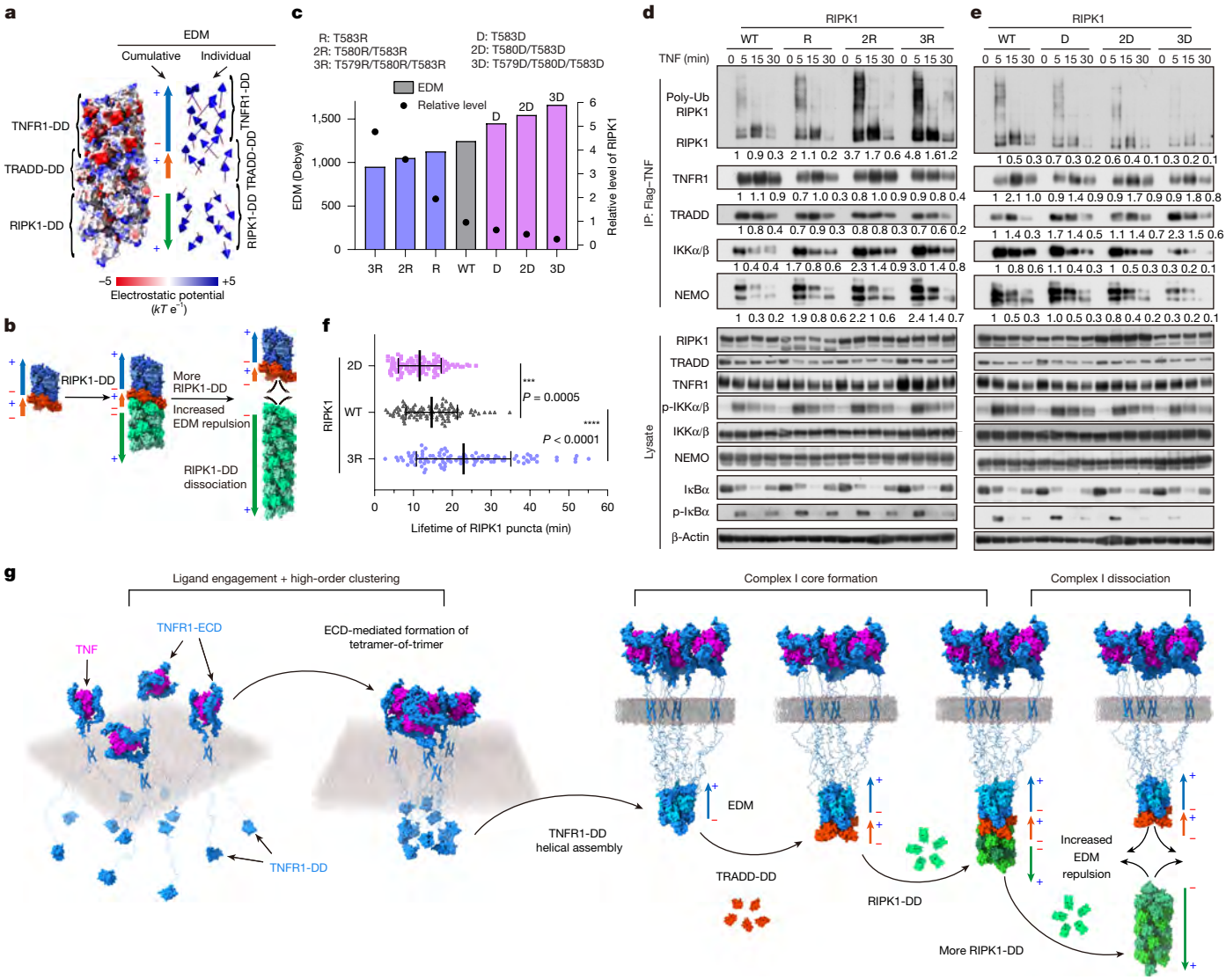


Fig. 5 | Regulation of complex I dynamics by protein EDM. a, EDMs of TNFR1-DD, TRADD-DD and RIPK1-DD layers (blue, orange and green, respectively) (left) and individual DD EDMs (right) in the superternary complex. All EDMs were calculated using the finite difference Poisson–Boltzmann method[22] under physiological conditions (150 mM NaCl at pH 7.0) to account for ionic screening effects[35]. **b**, Illustration of EDM-mediated attraction between TNFR1-DD and TRADD-DD, and repulsion between TNFR1-DD–TRADD-DD and RIPK1-DD in the superternary complex. **c**, Cumulative EDMs of one layer of DD pentamer for RIPK1-DD WT and variants with different charge substitutions at three sites (Thr579, Thr580 and Thr583) (bar) and the corresponding amount of recruited RIPK1 variants in complex I after TNF stimulation (100 ng ml^{-1}) for 5 min (black dot). **d**, Western blot analysis of complex I formation and NF-κB activation induced by TNF (100 ng ml^{-1}) in *RIPK1*-KO HeLa cells reconstituted with WT or EDM-decreased RIPK1 mutants. **e**, Western blot analysis of complex I formation and NF-κB activation induced by TNF (100 ng ml^{-1}) in *RIPK1*-KO HeLa cells reconstituted with WT or EDM-increased RIPK1 mutants. The relative levels of proteins normalized to β-actin are shown below the blots. **f**, Statistics of the lifetime of RIPK1 puncta on the cell membrane tracked by TIRF microscopy after TNF stimulation (100 ng ml^{-1}) in *RIPK1*-KO HeLa cells expressing WT RIPK1 or the indicated variants. Data are mean ± s.e.m. for 100 puncta in each group. **g**, Model of TNFR1 signalling. TNF binds to TNFR1, initiates its clustering to form tetramer-of-trimeric complexes and formation of DD pentamers, which seed the recruitment of TRADD-DD and RIPK1-DD. The cumulative EDM of RIPK1-DD layers exerts a repulsion between RIPK1-DD and TNFR1-DD–TRADD-DD, which causes the dissociation of RIPK1-DD. The results are representative of three independent experiments (**d**, **e** and **f**). *P* values in **f** were calculated using two-tailed Welch's *t*-tests for comparison between two groups; *$P < 0.05$, **$P < 0.01$, ***$P < 0.001$, ****$P < 0.0001$.

To further demonstrate the effect of EDM interaction on the dynamics of complex I in live cells, we tracked membrane-associated RIPK1 puncta in *RIPK1*-KO HeLa cells expressing mNeonGreen-tagged WT RIPK1 or EDM-modulated RIPK1 mutants. TIRF microscopy recorded time-lapse images of the complex I puncta induced by TNF in cells expressing the WT, 3R or 2D RIPK1 variants (Extended Data Fig. 7i). Single-puncta analysis revealed that the 3R mutant puncta on cell membrane exhibited substantially longer lifetime than the WT puncta, whereas the 2D mutant puncta have shorter lifetime than that of the WT (Fig. 5f and Extended Data Fig. 7j–l). This result indicates that weaker opposing EDM repulsion from the 3R RIPK1 mutant resulted in a substantially longer lifetime of complex I, whereas stronger EDM repulsion from the 2D mutant significantly reduced the complex I resident time, providing direct evidence that protein EDM regulates the dissociation kinetics of TNFR1-mediated complex I signalosome.

EDM has long been implicated in protein structure stability and function[22–24], but its function in modulating large signalling complexes has never been experimentally demonstrated. Here we show that the EDM interactions between the three types of DD pentamer layers provide a biophysical mechanism for the dynamic assembly and disassembly of complex I (Fig. 5g and Supplementary Video 1).

TNF engagement with TNFR1 promotes the clustering of trimeric TNFR1-ECD–TNF, mediated by the dimeric interaction of the pre-ligand association domain of TNFR1[25], on the cell membrane to initiate self-oligomerization of intracellular DD of TNFR1. The assembly of multiple layers of TNFR1-DD provides the seed for the rapid recruitment of TRADD-DD through energetically favourable interfacial charge complementation and EDM attraction. The TRADD-DD layer in turn acts as an adaptor to recruit RIPK1-DD through electrostatic complementation between the contact interfaces of TRADD-DD and RIPK1-DD pentamers. However, cumulative EDM generated by the RIPK1-DD pentamer layers opposes the EDMs of the TRADD-DD and TNFR1-DD layers, creating a point of instability at the TRADD-DD–RIPK1-DD interface. This instability leads to dynamic reversibility as EDM repulsion increases with the growth of the RIPK1-DD helical oligomers in the ternary complex. Taken together, our results support the model of dipole–dipole interaction in TNFR1-DD–TRADD-DD–RIPK1-DD helical oligomers that controls not only the rapid formation of complex I but also the instability that leads to timed release of RIPK1 from complex I (Fig. 5g).

Discussion

TNFR1 clustering on the membrane is important for its intracellular signal transduction[25–29]. However, the architecture of a basic or minimal unit of a productive TNFR1 cluster was not clear; nor do we understand the role of TNFR1 clustering in organizing the formation of its dynamic intracellular signalosome complex, complex I. Our structural and functional analyses indicate that the copies of TNFR1, TRADD and RIPK1 recruited into complex I may be dynamically regulated by the EDMs of the DD subunits of the superternary complex, providing an important intracellular mechanism to regulate the copy number of TNFR1 on the cell membrane to be recruited into active signalling complex. Furthermore, our functional analyses of the interplay between extracellular TNFR1-ECD clustering and intracellular TNFR1-DD assembly suggest that the basic activation unit for TNFR1 cluster consists of four trimeric TNFR1–TNF complexes. It is interesting that a transient intracellular signalling complex, that is, complex I, can exert powerful regulatory function in the formation of ligand-engaged receptor clustering on the cell membrane, providing an unappreciated aspect of the regulatory relationship between the ligand-engaged receptor and its intracellular signalling mechanism.

In this study, the role of EDM in regulating the recruitment of RIPK1 and other components in complex I is demonstrated by mutations designed to reduce/increase long-range EDM repulsion in the assembly without affecting DD–DD interacting interfaces. Our results indicate that decreasing or increasing the EDM of RIPK1-DD has the effect of increasing or decreasing the amount of RIPK1 recruited to complex I, respectively. In addition to limiting the copy number of RIPK1 recruited to complex I and thereby restricting the signalling strength of complex I, the EDM also defines the structural instability of complex I to lead to its disassembly, which is crucial to promote downstream NF-κB signalling in the nucleus. We also observed that intracellular assembly of complex I can restrict TNF–TNFR1 interaction on the cell surface (Extended Data Fig. 8a–i). Although the precise structural basis of the extracellular–intracellular coupling remains to be investigated, a plausible explanation is that complex I formation restricts the cluster size of TNFR1 by limiting the number of TNFR1-DD allowed in the complex I.

The dynamic assembly and disassembly of large receptor signalling complex after stimulation by cognate ligands is fundamental for the initiation and termination of all extracellular to intracellular signalling events. Our finding of EDM-mediated interactions between stacked layers of RIPK1-DD pentamers and TNFR1-DD–TRADD-DD provides an example for the role of long-range EDM interaction in the regulation of receptor signalling complex dynamics. EDM may provide a common structural principle for regulating the formation and dynamics of other signalling complexes. In cellular model studies, homo- or hetero-DD interactions are known to mediate cellular signalling[30]. In particular, DD oligomerization has been implicated in mediating FAS signalling through FAS–FADD interaction[31,32], in mediating MYD88–IRAK4–IRAK2 interactions after activation of the TLR/IL-1R family[33] and in the formation of the oligomeric PIDDosome complex[34]. Some of these systems show similar opposing EDMs (Extended Data Figs. 9 and 10). Thus, it will be interesting to examine the possible functional involvement of EDM as a common principle regulating the dynamic formation and dissolution of these signalling complexes in response to their cognate ligand stimulation.

Online content

Any methods, additional references, Nature Portfolio reporting summaries, source data, extended data, supplementary information, acknowledgements, peer review information; details of author contributions and competing interests; and statements of data and code availability are available at https://doi.org/10.1038/s41586-026-10304-1.

1. Micheau, O. & Tschopp, J. Induction of TNF receptor I-mediated apoptosis via two sequential signaling complexes. *Cell* **114**, 181–190 (2003).
2. Linkermann, A. & Green, D. R. Necroptosis. *N. Engl. J. Med.* **370**, 455–465 (2014).
3. Ofengeim, D. & Yuan, J. Regulation of RIP1 kinase signalling at the crossroads of inflammation and cell death. *Nat. Rev. Mol. Cell Biol.* **14**, 727–736 (2013).
4. Chen, G. & Goeddel, D. V. TNF-R1 signaling: a beautiful pathway. *Science* **296**, 1634–1635 (2002).
5. Bradley, J. R. TNF-mediated inflammatory disease. *J. Pathol.* **214**, 149–160 (2008).
6. Sun, Z. et al. Cooperation of TRADD- and RIPK1-dependent cell death pathways in maintaining intestinal homeostasis. *Nat. Commun.* **16**, 1890 (2025).
7. Jiang, Y., Woronicz, J. D., Liu, W. & Goeddel, D. V. Prevention of constitutive TNF receptor 1 signaling by silencer of death domains. *Science* **283**, 543–546 (1999).
8. Hsu, H., Huang, J., Shu, H. B., Baichwal, V. & Goeddel, D. V. TNF-dependent recruitment of the protein kinase RIP to the TNF receptor-1 signaling complex. *Immunity* **4**, 387–396 (1996).
9. Hsu, H., Xiong, J. & Goeddel, D. V. The TNF receptor 1-associated protein TRADD signals cell death and NF-κB activation. *Cell* **81**, 495–504 (1995).
10. Dondelinger, Y., Darding, M., Bertrand, M. J. & Walczak, H. Poly-ubiquitination in TNFR1-mediated necroptosis. *Cell. Mol. Life Sci.* **73**, 2165–2176 (2016).
11. Li, X. et al. Ubiquitination of RIPK1 regulates its activation mediated by TNFR1 and TLRs signaling in distinct manners. *Nat. Commun.* **11**, 6364 (2020).
12. Wertz, I. E. & Dixit, V. M. Ubiquitin-mediated regulation of TNFR1 signaling. *Cytokine Growth Factor Rev.* **19**, 313–324 (2008).
13. Iwai, K. LUBAC-mediated linear ubiquitination: a crucial regulator of immune signaling. *Proc. Jpn Acad. Ser. B* **97**, 120–133 (2021).
14. Mifflin, L., Ofengeim, D. & Yuan, J. Receptor-interacting protein kinase 1 (RIPK1) as a therapeutic target. *Nat. Rev. Drug Discov.* **19**, 553–571 (2020).
15. Sukits, S. F. et al. Solution structure of the tumor necrosis factor receptor-1 death domain. *J. Mol. Biol.* **310**, 895–906 (2001).
16. Zhang, N., Yuan, W., Fan, J. S. & Lin, Z. Structure of the C-terminal domain of TRADD reveals a novel fold in the death domain superfamily. *Sci. Rep.* **7**, 7073 (2017).
17. Ding, J. et al. Structural and functional insights into host death domains inactivation by the bacterial arginine GlcNAcyltransferase effector. *Mol. Cell* **74**, 922–935 (2019).
18. Hsu, H., Shu, H. B., Pan, M. G. & Goeddel, D. V. TRADD-TRAF2 and TRADD-FADD interactions define two distinct TNF receptor 1 signal transduction pathways. *Cell* **84**, 299–308 (1996).
19. Vangone, A. & Bonvin, A. M. Contacts-based prediction of binding affinity in protein-protein complexes. *eLife* **4**, e07454 (2015).
20. Lim, C. S., Lee, J., Kim, J. W. & Lee, J. O. Highly ordered clustering of TNFα and BAFF ligand-receptor-intracellular adaptor complexes on a lipid membrane. *Nat. Commun.* **16**, 5551 (2025).
21. Zhao, L., Fu, Q., Pan, L., Piai, A. & Chou, J. J. The diversity and similarity of transmembrane trimerization of TNF receptors. *Front. Cell Dev. Biol.* **8**, 569684 (2020).
22. Sharp, K. A. & Honig, B. Electrostatic interactions in macromolecules: theory and applications. *Annu. Rev. Biophys. Biophys. Chem.* **19**, 301–332 (1990).
23. Warshel, A. & Papazyan, A. Electrostatic effects in macromolecules: fundamental concepts and practical modeling. *Curr. Opin. Struct. Biol.* **8**, 211–217 (1998).
24. Lockhart, D. J. & Kim, P. S. Internal stark effect measurement of the electric field at the amino terminus of an alpha helix. *Science* **257**, 947–951 (1992).
25. Chan, F. K. et al. A domain in TNF receptors that mediates ligand-independent receptor assembly and signaling. *Science* **288**, 2351–2354 (2000).
26. Karathanasis, C. et al. Single-molecule imaging reveals the oligomeric state of functional TNFα-induced plasma membrane TNFR1 clusters in cells. *Sci. Signal.* **13**, eaax5647 (2020).
27. Chan, F. K. The pre-ligand binding assembly domain: a potential target of inhibition of tumour necrosis factor receptor function. *Ann. Rheum. Dis.* **59**, i50–i53 (2000).
28. Naismith, J. H., Devine, T. Q., Brandhuber, B. J. & Sprang, S. R. Crystallographic evidence for dimerization of unliganded tumor necrosis factor receptor. *J. Biol. Chem.* **270**, 13303–13307 (1995).

29. Kucka, K. & Wajant, H. Receptor oligomerization and its relevance for signaling by receptors of the tumor necrosis factor receptor superfamily. *Front. Cell Dev. Biol.* **8**, 615141 (2020).
30. Ferrao, R. & Wu, H. Helical assembly in the death domain (DD) superfamily. *Curr. Opin. Struct. Biol.* **22**, 241–247 (2012).
31. Wang, L. et al. The Fas-FADD death domain complex structure reveals the basis of DISC assembly and disease mutations. *Nat. Struct. Mol. Biol.* **17**, 1324–1329 (2010).
32. Scott, F. L. et al. The Fas-FADD death domain complex structure unravels signalling by receptor clustering. *Nature* **457**, 1019–1022 (2009).
33. Lin, S. C., Lo, Y. C. & Wu, H. Helical assembly in the MyD88-IRAK4-IRAK2 complex in TLR/IL-1R signalling. *Nature* **465**, 885–890 (2010).
34. Park, H. H. et al. Death domain assembly mechanism revealed by crystal structure of the oligomeric PIDDosome core complex. *Cell* **128**, 533–546 (2007).
35. Bertonati, C., Honig, B. & Alexov, E. Poisson-Boltzmann calculations of nonspecific salt effects on protein-protein binding free energies. *Biophys. J.* **92**, 1891–1899 (2007).

Publisher's note Springer Nature remains neutral with regard to jurisdictional claims in published maps and institutional affiliations.

Springer Nature or its licensor (e.g. a society or other partner) holds exclusive rights to this article under a publishing agreement with the author(s) or other rightsholder(s); author self-archiving of the accepted manuscript version of this article is solely governed by the terms of such publishing agreement and applicable law.

© The Author(s), under exclusive licence to Springer Nature Limited 2026

Methods

Antibodies

The following polyclonal antibodies from Cell Signaling Technology were used in immunoblotting at dilution rate recommended by suppliers: anti-IKKa (2682), anti-IKKb (2370), anti-IkBa (4812), anti-pIkBa (9246), anti-p-IKKa/b (2078), anti-hTNFR1 (3736), anti-TRADD (3694), anti-NEMO (79154), anti-β-actin (4967). Rabbit anti-hRIPK1 (BX60006) polyclonal antibody is from Biolynx Biotech (Hangzhou, China). Mouse anti-β-tubulin monoclonal antibodies (HC101-01) were obtained from TransGen Biotech (Beijing, China).

Plasmids

For bacterial expression of ternary DD complex, DNA sequences encoding the death domains of human TNFR1(342–455), TRADD(199–312) or RIPK1(560–671) were cloned into three modified pET32a, pRSF-Deut1 or pAcyc-Deut1 vectors (Novagen) with different antibiotic resistance, and fused to an N-terminal GST, or 6 × His-GB1 tag. Point mutations were introduced into target gene by PCR. TNFR1-DD and RIPK1-DD mutants were fused to an N-terminal 6 × His-SUMO, 6 × His-MBP, 6 × His or 6 × His-GB1 tag as indicated for expression in *E. coli*. An HRV 3c protease recognition motif (LEVLFQGPGS) was introduced before DD to enable cleavage of the fusion tag. The genes encoding the Nb70 nanobody[36] and ALFA-nanobody[37] (with the S23C mutation) were synthesized (Tsingke Biotech) and cloned into pET22b with an N-terminal 6×His-SUMO tag. For transient expression of TNFR1-DD, TRADD-DD or RIPK1-DD, DNA sequences encoding the DDs were inserted into a pCMV vector (Clontech) with either an mEGFP or mCherry tag fused to their N termini. For stable expression of full-length TNFR1, TRADD or RIPK1 in cells, synonymous replacement of the guide RNA sequence was introduced into full-length gene cloned into pMSCV vector (TaKaRa Bio) to make viral expression constructs. Fluorescent tag or Halo tag were fused to the C terminus of full-length TNFR1 or the N terminus of full-length TRADD and RIPK1. All constructs were verified by DNA sequencing,

Protein expression and purification

All of the DD fusion proteins were expressed in *E. coli* BL21(DE3). For co-expression of TNFR1-DD–TRADD-DD–RIPK1-DD complexes, plasmids containing coding regions for different DDs were co-transformed into BL21(DE3) cells. The bacteria were cultured until the optical density at 600 nm (OD_{600}) reached around 1.0 and transferred to 16 °C incubator to cool down for 30 min, then induced with 0.1 mM IPTG for 20 h to express target proteins. His-SUMO-tagged Nb70[36] or ALFA nanobody[37] and Flag-tagged or ALFA-tagged hTNF(77–233) were produced in *E. coli* with the same method as that for DD proteins.

The induced *E. coli* cells were collected by centrifugation and disrupted in binding buffer (50 mM Tris-HCl, pH 8.0, 500 mM NaCl, 5 mM imidazole) with a high-pressure homogenizer. The supernatant of lysate centrifugated at 15,000 rpm (Backmann JA20 rotor) for 40 min was incubated with Ni^{2+} or GST affinity beads (Smart Life-sciences) for 30 min. After extensive washing with binding buffer, the fusion protein was eluted with elution buffer (50 mM Tris-HCl, pH 8.0, 500 mM NaCl, 200 mM imidazole) and further purified on a size-exclusion column (Superdex 200 Increase 10/300 or Superdex 200 26/60, Cytiva) with buffer A (20 mM Tris-HCl, pH 7.5, 100 mM NaCl, 1 mM EDTA, 1 mM DTT). The peak fractions were collected and subjected to SDS–PAGE to check the purity.

For fluorescent dye conjugation, 100 μM S23C mutated ALFA nanobody was purified in PBS buffer and incubated with AlexaFluor 647 C5 maleimide (Thermo Fisher) in 1:3 molar ratio for at 4 °C protected from light. After a 12 h reaction, 1 mM reduced glutathione was added to consume the excessive dye. The dye-conjugated nanobody was separated from free dye by size-exclusion chromatography using the Superdex 75 column (Cytiva) in PBS buffer.

GST pull-down

Purified GST–TNFR1-DD protein (50 μg) was incubated with 5 μl glutathione agarose beads (Smart-Lifesciences) for 30 min at 16 °C and washed three times with buffer A (20 mM Tris-HCl, pH 7.5, 100 mM NaCl, 1 mM EDTA, 1 mM DTT), then mixed with 100 μg SUMO-TRADD-DD and/or 100 μg GB1–RIP1-DD proteins for 30 min at 16 °C. The beads were then washed three times with buffer A to remove unbound proteins, then boiled in 30 μl 2× SDS–PAGE sample buffer for 2 min. Denatured proteins were separated by SDS–PAGE in 15% polyacrylamide gel and stained with Coomassie blue R250.

Preparation of electron microscopy specimen

To trigger the formation of individual DD protein fibres (TNFR1-DD, TRADD-DD or RIPK1-DD), the fusion tag was cut from DD protein by HRV 3c protease overnight on ice without further separation of tag. For negative staining, a drop of 5 μl protein (0.01–0.1 mg ml^{-1}) was applied onto the graphene-covered copper grid and negative stained with 2% (w/v) uranyl acetate. Negative-stained specimens were examined on the 120-kV Tecnai T12 transmission electron microscope (FEI). To generate the cryo-EM specimen, a drop of 5 μl protein sample (2–3 mg ml^{-1}) was applied to glow-discharged (Harrick Plasma) 200 mesh holey carbon Au 2/1 grids (Quantifoil) for 5 s absorption, then the grids were blotted with filter paper for 1.5 s with a blot force setting of −2 in the chamber of the Vitrobot Mark IV (Thermo Fisher Scientific), which was maintained at 4 °C and 100% humidity. The grids were plunged into liquid ethane bathed in liquid nitrogen to vitrify the protein sample. Grids were screened and imaged on the 300-kV Titan Krios G4 electron microscope (Thermo Fisher Scientific), equipped with a Biocontinuum K3 direct electron detector with GIF filter (Gatan). Video stacks were recorded using EPU software (Thermo Fisher Scientific) using the settings shown in Extended Data Table 1. Each video was recorded at a dose rate of 25 electrons per pixel per second with an accumulated exposure of 2.2 s fractionated into 40 frames.

Micrograph processing

Cryo-EM videos and images were processed in RELION (v.3.1)[38] and CryoSPARC (v.4.6.2)[39]. Video stacks were motion corrected with dose-weighting correction in RELION. Contrast transfer function (CTF) parameters were determined using patch CTF estimation. For the TNFR1-DD, TRADD-DD or RIPK1-DD individual protein fibres, well-separated and straight portion of filaments were traced and picked in micrographs in RELION or CryoSPARC, then extracted into boxes of 400 × 400 pixels. After two-dimensional classification. Particles in the largest class were selected for three-dimensional classification using the ab initial volume derived from a small subset as a reference template. A good set of particles that generated a volume with clear helical features were selected to refine the volume with imposed helical symmetry parameters as shown in Extended Data Table 1. Similar processing steps was applied to the micrographs of TNFR1-DD–TRADD-DD–RIPK1-DD ternary complex; however, the single-particle reconstruction method was adopted to generate the volume density. The overall volume resolution was further improved with local motion correction and local CTF refinement. A summary of the processing details is provided in Extended Data Table 1. All EM density volumes were visualized using ChimeraX[40].

Model building and refinement

The monomeric DD structures of TNFR1-DD, TRADD-DD, RIPK1-DD and FADD-DD (Protein Data Bank (PDB): 1ICH, 6AC0, 6AC5 and 6ACI) were used to search for multiple copies in the cryo-EM volume by rigid fitting into an EM map using Phenix software[41]. Models were further improved by several cycles of manual adjustment and real-space refinement against EM map in Phenix[4]. Structure images were made in the programs PyMOL or Chimera X (v.1.9)[40].

Calculation of EDM

In this work, the method for calculating EDMs of DD domains or layers is described previously[42]. To take into account ionic screening effect on protein in solution, the ionic charge distribution around the ternary DD complex was calculated with adaptive Poisson-Boltzmann solver (APBS)[43]. First, partial atomic charges of protein in vacuum were assigned to each atom using the PDB2PQR software[44]. Next, the ternary DD complex was solvated in a box (145.32 Å × 148.59 Å × 322.88 Å) of 150 mM NaCl solution, which was divided into a set of 129 × 129 × 289 grids. The ionic charge density in the system was solved using the nonlinear Poisson–Boltzmann equation in APBS. The contribution of EDM from solution ions within the distance of one unit of Debye length (8 Å) from the protein surface was calculated by the same method used for the protein. Specifically, the centre of mass of the protein was computed based on the atomic coordinates of all protein atoms. Dipole vectors for protein atoms were calculated by multiplying the protein atomic charge ($q_{\mathrm{pro},i}$) by the vector from the atom position ($\mathbf{r}_{\mathrm{pro},i}$) to the centre of mass $\mathbf{r}_{\mathrm{c}}$ dipole, vectors for solution grids within one Debye length (8 Å) from protein surface were calculated by multiplying the ionic charge ($q_{\mathrm{ion},j}$) by the vector from the grid's position ($\mathbf{r}_{\mathrm{ion},j}$) to the centre of mass ($\mathbf{r}_{\mathrm{c}}$). Finally, the total EDM was obtained by summing the contributions from protein atoms and solution ionic charge around proteins, as defined by the following equation, with a constant applied to convert the result to Debye units:

$$\mathrm{EDM} = 4.8032 \times \left[\sum_i (\mathbf{r}_{\mathrm{pro},i} - \mathbf{r}_{\mathrm{c}}) q_{\mathrm{pro},i} + \sum_j (\mathbf{r}_{\mathrm{ion},j} - \mathbf{r}_{\mathrm{c}}) q_{\mathrm{ion},j} \right]$$

Modelling of TNF engaged TNFR1 in complex with TRADD-DD–RIPK1-DD on the membrane

The TMD domain structure from PDB 7K7A was inserted into a membrane generated using CHARMM-GUI[45]. The loops between the ECD, TMD and DD were generated using AlphaFold and linked to the ternary DD complex and TNFR1-ECD–TNF complex structure model, which was built by docking TNF (PDB: 7KP7) and TNFR1-ECD (PDB: 1NCF) into the density volume (EMD-60497). The model was built in Coot[46] to maintain realistic bond lengths and angles to avoid steric clash.

Gene KO and cell lines

TNFR1-, *TRADD*- or *RIPK1*-KO HeLa cells were made using CRISPR–Cas9 technology with the following guide RNA sequences: *TNFR1* (GGAC CAGTCCAATAACCCCTG), *RIPK1* (GGCACCGCTAAGAAGAATGG) and *TRADD* (GGCCGCGCTCGCCCAGCACTCGG).

For retroviral expression of *TNFR1*, *TRADD* or *RIPK1* variants in corresponding HeLa KO cells, synonymous replacement of the guide RNA sequence in these genes was introduced into their respective pMSCV constructs (with blasticidin selection marker) to avoid Cas9 cutting. Recombinant murine stem cell retroviruses (MSCV) produced with these constructs were used to infect cells for stable expression of target genes. For reconstitution with two complementary mutants (for example, R376E TNFR1 + E398R TNFR1 or E620R RIPK1 + R621E RIPK1), cells were co-infected with two viruses for 24 h and expanded to the desired quantity for downstream assays without further selection.

Tissue culture, transfection and viral infection

All cell lines were cultured at 37 °C with 5% CO_2 in Dulbecco's modified Eagle's medium (Gibco; Thermo Fisher Scientific) with 4.5 g l^{-1} glucose, 4 mM L-glutamine and additional supplement of 10% FBS (Gibco; Thermo Fisher Scientific) and antibiotics (100 U ml^{-1} penicillin G and 100 mg ml^{-1} streptomycin) (MesGen Biotech). Transient transfections of HeLa cells were performed using polyethylenimine (PEI, 23966; Polysciences) according to the instructions of the reagent vendor. Cells were plated in a 12-well plate at a density of 5×10^4 cells per well and transfected with a total of 1 μg DNA per well for 24 h.

For viral infection of HeLa cells, recombinant mouse stem cell retroviruses were prepared from HEK293T cells according to the standard protocol of pMSCV vector supplier (TaKaRa Bio). Viral particles in the culture supernatant were filtered through a 0.45-μm filter and mixed with polybrene (8 μg ml^{-1}) before adding to cells. After 24 h infection, cells stably expressing target genes were selected in medium with 10 μg ml^{-1} blasticidin for 3 days.

Immunoprecipitation and western blotting

TNFR1 complex I immunoprecipitation was performed as previously described[1,47,48]. Each 15 cm dish of cells was washed twice with cold PBS and scraped down in 1.0 ml NP40 lysis buffer containing 50 mM Tris-HCl pH 7.5, 150 mM NaCl, 1%(v/v) Nonidet P40, 5 mM NaF, 5 mM *N*-ethylmaleimide, 1 mM Na_3VO_4, 10%(v/v) glycerol, 1 × EDTA-free protease inhibitor cocktail (Amresco), 1 mM PMSF and 10 mM β-glycerophosphate. After lysis for 1 h at 4 °C with continuous inversion, the lysates was cleared by centrifugation at 20,000*g* for 15 min at 4 °C. The supernatant was incubated with 5 μl anti-Flag M2 agarose beads (Sigma-Aldrich) and with continuous inversion for 4 h at 4 °C. Beads were washed four times with 1 ml wash buffer containing 50 mM Tris-HCl pH 7.5, 150 mM NaCl, 1%(v/v) Nonidet P40. Precipitated proteins were denatured with 70 μl 2× SDS–PAGE sample buffer at 65 °C for 5 min. Both lysate and IP samples were analysed using SDS–PAGE in 10% gel. The protein bands were transferred to nitrocellulose membrane for detection using primary antibodies. HRP-conjugated goat-anti-rabbit IgG or goat-anti-mouse IgG (Thermo Fisher Scientific) were used to amplify the signal by chemiluminescence method.

For Nb70 competitional immunoprecipitation assay, HeLa cells were pretreated with Nb70 nanobody for 30 min before Flag–TNF stimulation for 10 min. The TNF-bound TNFR1 was co-immunoprecipitated using the same method for complex I.

RT–qPCR

Total RNA was extracted from cells using TRIzol reagent (Invitrogen) according to the vendor's instructions. The quantity and purity of isolated RNA were assessed using the NanoDrop 2000 spectrophotometer (Thermo Fisher Scientific). Total RNA was used to synthesize cDNA using a reverse transcription kit (HiScript IV All-in-One Ultra RT SuperMix for qPCR, R433, Vazyme). The resulting cDNA was used as template for qPCR using a commercial kit (ChamQ SYBR qPCR Master Mix, Q311, Vazyme) to amplify target genes using the QuantStudio 7 Flex Real-Time PCR system (Life Technologies). The primers for *A20* and *ACTB* were as follows: A20_F TCCTCAGGCTTTGTATTTGAGC, A20_R TGTGTATCGGTGCATGGTTTTA, ACTB_F CATGTACGTTGCTATCCAGGC and ACTB_R CTCCTTAATGTCACGCACGAT. The gene expression levels of *A20* and reference gene *ACTB* were determined using the $\Delta\Delta C_t$ method.

Fluorescence microscopy

HeLa cells were seeded onto poly-L-lysine-coated glass cover slips in a 12-well plate at a density of 2×10^4 cells per well, and transfected with respective plasmids using polyethylenimine (PEI). Cells were washed with PBS, fixed with 4% paraformaldehyde and permeabilized with 0.1% Triton X-100. Nuclear DNA was stained with DAPI (Sigma-Aldrich). Cells expressing mEGFP- or mCherry-tagged DD proteins were imaged using the DMi8 confocal microscope (Leica) using a ×40 objective lens. Images were taken using the Leica application suite X software and processed in Fiji[49].

Fluorescence-activated cell sorting

HeLa cells were detached from culture dishes by trypsin-EDTA digestion, then resuspended in warm PBS and stimulated for 10 min at 37 °C with 100 ng ml^{-1} ALFA-tagged TNF, which was pre-incubated with AlexaFlour-647-conjugated anti-ALFA nanobody (1:1 molar ratio).

The stimulated and unstimulated control cells were then sorted using a flow cytometer (Northern Lights, Cytek). Fluorescence-activated cell sorting data were analysed using FlowJo (https://www.flowjo.com).

TIRF microscopy

For imaging of RIPK1 recruitment on cell membrane, *RIPK1*-KO HeLa cells expressing mNeonGreen-tagged RIPK1 variants were plated in 35-mm glass-bottom dishes (Cellvis) 24 h before live imaging. Human TNF diluted in warm DMEM medium was added at the indicated final concentration. The microscope chamber was maintained under physiological conditions (37 °C, 5% CO_2). Time-lapse imaging of cells was conducted using the HIS-SIM microscope (CSR Biotech) in TIRF mode using a ×100/1.5 NA oil-immersion objective lens to track RIPK1 on cell membrane for 1 h.

For TNFR1 clustering analysis, *TNFR1*-KO HeLa cells transfected with mNeonGreen-tagged or Halo-tagged TNFR1 variants were cultured on 35 mm glass coverslips with phenol red-free imaging buffer. For cells expressing Halo-tagged TNFR1, 10 nM Halo tag TMR dye (HY-D2270, MedChemExpress) was added to cells 10 min before stimulation with TNF (20 ng ml^{-1}). After 5 min of stimulation, the cells were washed with PBS, fixed with 4% paraformaldehyde (PFA) for 15 min and then washed with PBS. The cells were then imaged with a HIS-SIM microscope (CSR Biotech) in TIRF mode using 488 nm laser excitation (for mNeonGreen) or 561 nm laser excitation (for Halo tag TMR) and with a ×100/1.47 NA oil-immersion objective lens. All images were processed using Fiji software[49] and the puncta of TNFR1 or RIPK1 were analysed using the ComDet v.0.5.5 plugin (https://github.com/UU-cellbiology/ComDet).

RNA-seq analysis

Total RNA of HeLa cells was extracted using TRIzol reagent according to the vendor's instructions (Invitrogen). The purity and quantity of RNA samples were assessed using the NanoDrop 2000 spectrophotometer (Thermo Fisher Scientific). RNA integrity was evaluated with Agilent 2100 Bioanalyzer (Agilent Technologies). The cDNA libraries for sequencing were prepared using the VAHTS Universal V6 RNAseq Library Prep Kit according to the manufacturer's protocol (Vazyme Biotech). The transcriptome sequencing and analysis were conducted by OE Biotech. Sequencing was conducted on the Illumina Novaseq 6000 platform (Illumina), which generated around 25 million 150 bp paired-end reads for each sample. Raw reads were processed using fastp package to remove the low-quality reads and obtain about 24 million clean reads for each sample for downstream analysis[50]. The clean reads were mapped to around 16,300 genes in the reference genome using HISAT2 package[51]. Fragments per kilobase of transcript per million mapped fragments (FPKM) and read counts were calculated using the HTSeq-count package[52,53]. Gene-level differential expression was quantified and tested using a negative binomial model in the package DESeq2[54]. Specifically, the genes upregulated more than twofold (with $q < 0.05$) in *RIPK1*-KO or *TNFR1*-KO HeLa cells reconstituted with WT *RIPK1* or *TNFR1* after 60 min TNF stimulation (compared with the unstimulated control cells) were considered to be TNF-induced genes. Two-tailed Welch's *t*-tests were used as the statistical method for comparisons. Only TNF-induced genes with a significant difference ($P < 0.05$) between the WT and mutant groups were used to generate the heat maps.

Material availability

Any additional information and reagents required to re-analyse the data reported in this paper are available from the corresponding author on request.

Reporting summary

Further information on research design is available in the Nature Portfolio Reporting Summary linked to this article.

Data availability

The atomic coordinates and cryo-EM density maps reported in this study have been deposited in the Protein Data Bank and Electron Microscopy Data Bank under accession codes 9V9C and EMD-64869 (TNFR1-DD filament), 9VGD and EMD-65047 (TRADD-DD filament), 9V9E and EMD-64870 (RIPK1-DD filament) and 9VIN and EMD-65094 (TNFR1-DD–TRADD-DD–RIPK1-DD ternary complex). Source data are provided with this paper.

36. Steeland, S. et al. Generation and characterization of small single domain antibodies inhibiting human tumor necrosis factor receptor 1. *J. Biol. Chem.* **290**, 4022–4037 (2015).
37. Götzke, H. et al. The ALFA-tag is a highly versatile tool for nanobody-based bioscience applications. *Nat. Commun.* **10**, 4403 (2019).
38. Scheres, S. H. RELION: implementation of a Bayesian approach to cryo-EM structure determination. *J. Struct. Biol.* **180**, 519–530 (2012).
39. Punjani, A., Rubinstein, J. L., Fleet, D. J. & Brubaker, M. A. cryoSPARC: algorithms for rapid unsupervised cryo-EM structure determination. *Nat. Methods* **14**, 290–296 (2017).
40. Pettersen, E. F. et al. UCSF Chimera—a visualization system for exploratory research and analysis. *J. Comput. Chem.* **25**, 1605–1612 (2004).
41. Liebschner, D. et al. Macromolecular structure determination using X-rays, neutrons and electrons: recent developments in Phenix. *Acta Crystallogr. D* **75**, 861–877 (2019).
42. Felder, C. E., Prilusky, J., Silman, I. & Sussman, J. L. A server and database for dipole moments of proteins. *Nucleic Acids Res.* **35**, W512–W521 (2007).
43. Baker, N. A., Sept, D., Joseph, S., Holst, M. J. & McCammon, J. A. Electrostatics of nanosystems: application to microtubules and the ribosome. *Proc. Natl Acad. Sci. USA* **98**, 10037–10041 (2001).
44. Dolinsky, T. J., Nielsen, J. E., McCammon, J. A. & Baker, N. A. PDB2PQR: an automated pipeline for the setup of Poisson-Boltzmann electrostatics calculations. *Nucleic Acids Res.* **32**, W665–W667 (2004).
45. Jo, S., Kim, T., Iyer, V. G. & Im, W. CHARMM-GUI: a web-based graphical user interface for CHARMM. *J. Comput. Chem.* **29**, 1859–1865 (2008).
46. Emsley, P. & Cowtan, K. Coot: model-building tools for molecular graphics. *Acta Crystallogr. D* **60**, 2126–2132 (2004).
47. Heger, K. et al. OTULIN limits cell death and inflammation by deubiquitinating LUBAC. *Nature* **559**, 120–124 (2018).
48. Lafont, E. et al. TBK1 and IKK ε prevent TNF-induced cell death by RIPK1 phosphorylation. *Nat. Cell Biol.* **20**, 1389–1399 (2018).
49. Schindelin, J. et al. Fiji: an open-source platform for biological-image analysis. *Nat. Methods* **9**, 676–682 (2012).
50. Chen, S., Zhou, Y., Chen, Y. & Gu, J. fastp: an ultra-fast all-in-one FASTQ preprocessor. *Bioinformatics* **34**, i884–i890 (2018).
51. Kim, D., Langmead, B. & Salzberg, S. L. HISAT: a fast spliced aligner with low memory requirements. *Nat. Methods* **12**, 357–360 (2015).
52. Anders, S., Pyl, P. T. & Huber, W. HTSeq—a Python framework to work with high-throughput sequencing data. *Bioinformatics* **31**, 166–169 (2015).
53. Roberts, A., Trapnell, C., Donaghey, J., Rinn, J. L. & Pachter, L. Improving RNA-seq expression estimates by correcting for fragment bias. *Genome Biol.* **12**, R22 (2011).
54. Love, M. I., Huber, W. & Anders, S. Moderated estimation of fold change and dispersion for RNA-seq data with DESeq2. *Genome Biol.* **15**, 550 (2014).

Acknowledgements We thank M. Zhang for his help in electroscope maintenance and training; Y. Ge for her help in fluorescence microscope maintenance and training; and H. Jing and B. Shan for discussion about RNA-seq. Funding: this project was supported (to J.Y.) by the China National Natural Science Foundation (82188101), the Shanghai Municipal Science and Technology Major Project (grant no. 2019SHZDZX02), the Shanghai Science and Technology Development Funds (22JC1410400) and the Shanghai Key Laboratory of Aging Studies (19DZ2260400). J.J.C. was funded by the Science and Technology Commission of Shanghai Municipality (22JC1410500), the Strategic Priority Research Program of the Chinese Academy of Sciences (XDB10060000) and the National Natural Science Fund of China-Research Fund for International Scientists (82350710799). J.L. was supported by a grant from the National Natural Science Foundation of China (32071297).

Author contributions J. Yuan conceptualized and directed the project. J.L., J.J.C. and J. Yuan designed research. J.L., J.Z. and J.G. purified proteins, performed biochemical and cell biology studies. J.L. solved TRADD-DD filament and ternary DD complex structures with help from Y.H. in data collection. K.Z. solved the cryo-EM structures of RIPK1-DD and TNFR1-DD filaments with samples prepared by J.L.; J. Yang calculated Gibbs free energy and EDM of DDs. F.W., X.L., Zekai Li and B.L. helped in protein expression and purification. S.J. helped in cell biology studies. Zefei Li, J. Ye and Z.S. contributed cell lines. J.L., J.Z., J.G., K.Z., J. Yang, C.L., Y.Z., J.J.C. and J. Yuan analysed data. J.L., J.Z., J.G., J. Yang, J.J.C. and J. Yuan wrote the paper.

Competing interests The authors declare no competing interests.

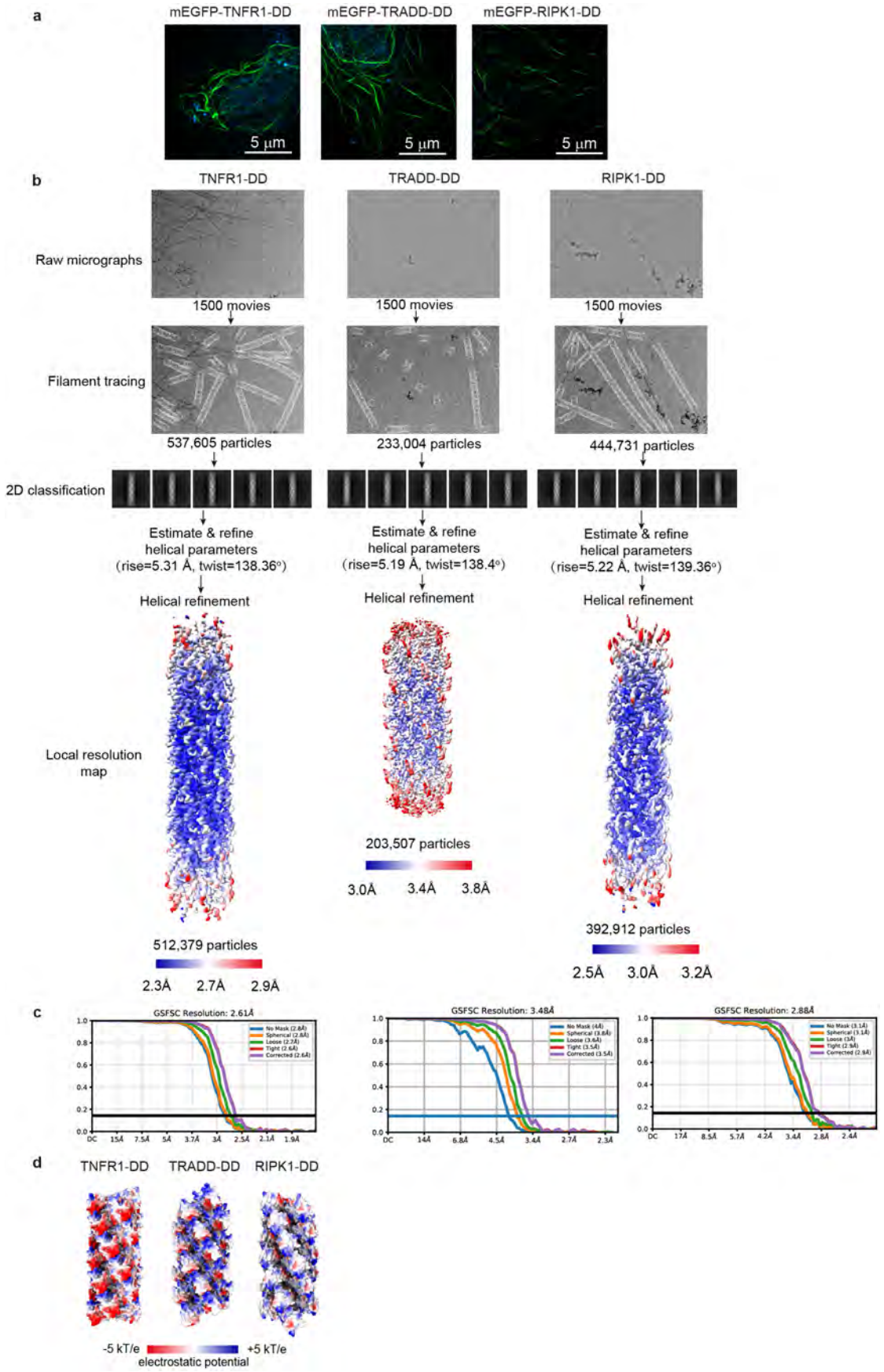
Additional information

Supplementary information The online version contains supplementary material available at https://doi.org/10.1038/s41586-026-10304-1.

Correspondence and requests for materials should be addressed to Jianping Liu, Junying Yuan or James J. Chou.

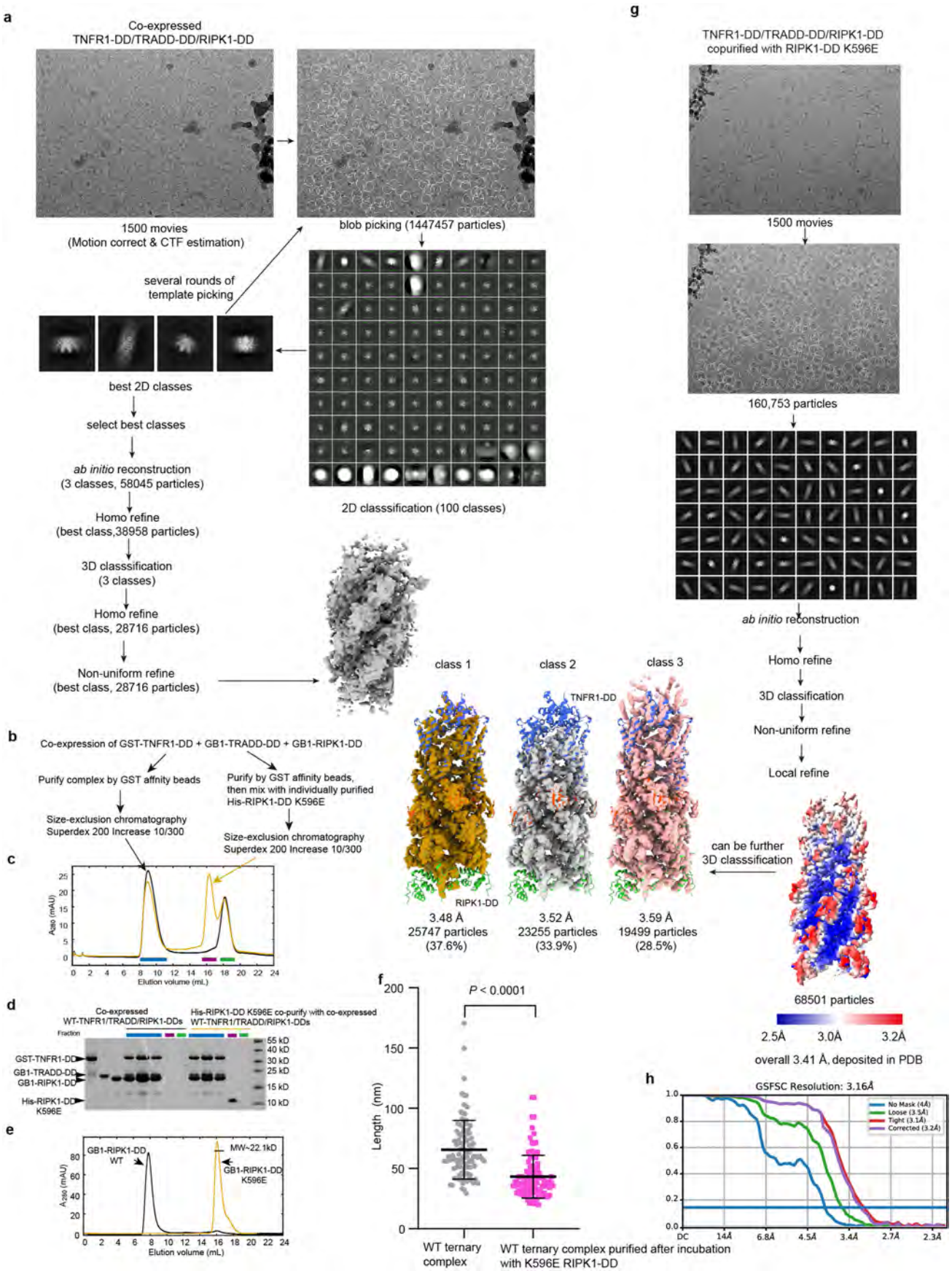
Peer review information *Nature* thanks the anonymous reviewers for their contribution to the peer review of this work. Peer reviewer reports are available.

Reprints and permissions information is available at http://www.nature.com/reprints.



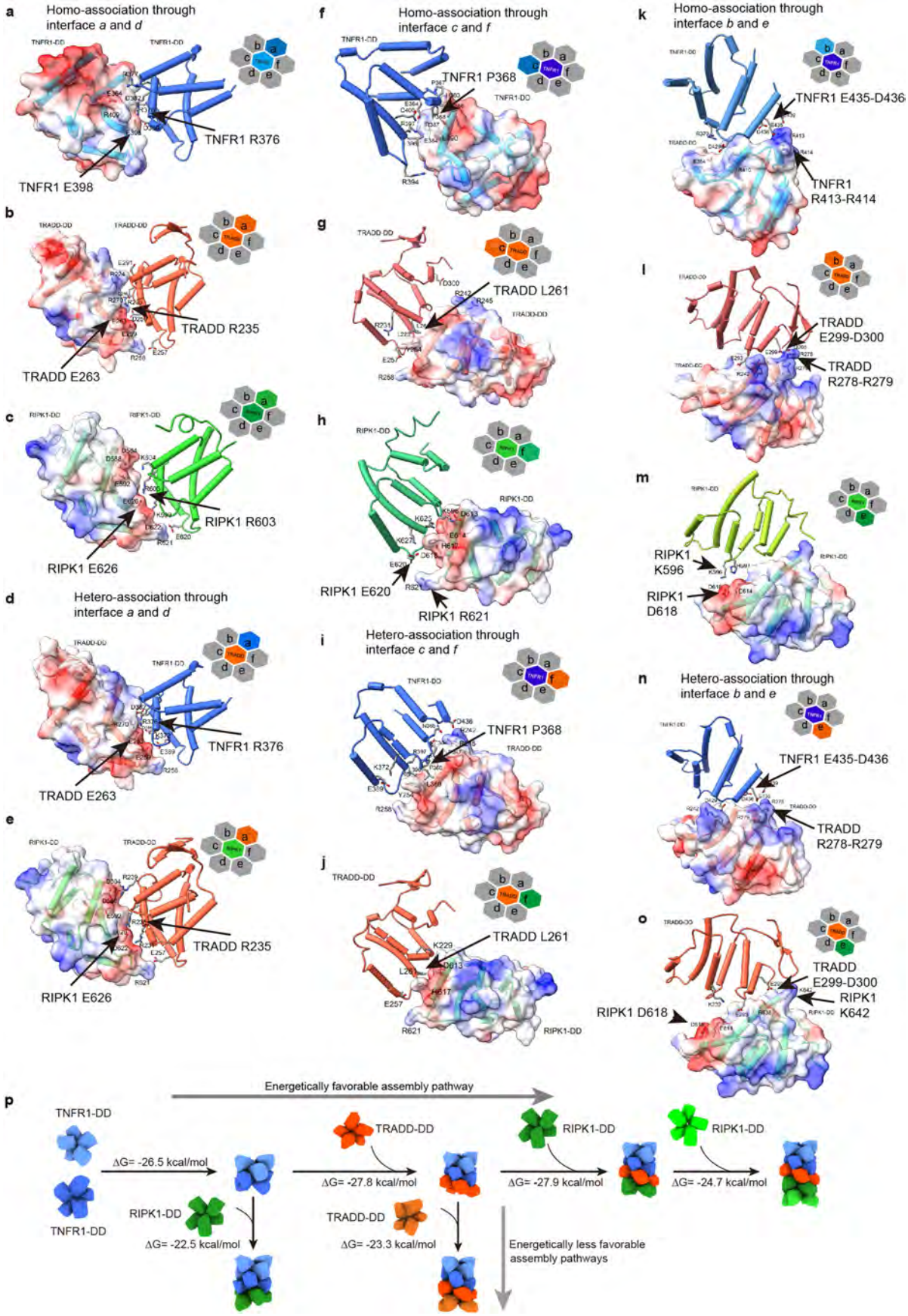
Extended Data Fig. 1 | See next page for caption.

Extended Data Fig. 1 | Cryo-EM structure determination of TNFR1-DD, TRADD-DD and RIPK1-DD helical filaments. a, Fluorescence images of HeLa cells expressing mEGFP-tagged TNFR1-DD, TRADD-DD or RIPK1-DD. **b**, Flow chart for the cryo-EM structure determination of TNFR1-DD, TRADD-DD, RIPK1-DD filaments and the local resolution filtered map calculated with FSC 0.143 criterion. **c**, The FSC curve calculated between two half maps of the refined final density volume. **d**, Electrostatic potential surface representation of the cryo-EM structures of TNFR1-DD, TRADD-DD and RIPK1-DD filaments. Results are representative of three independent experiments for (**a**).



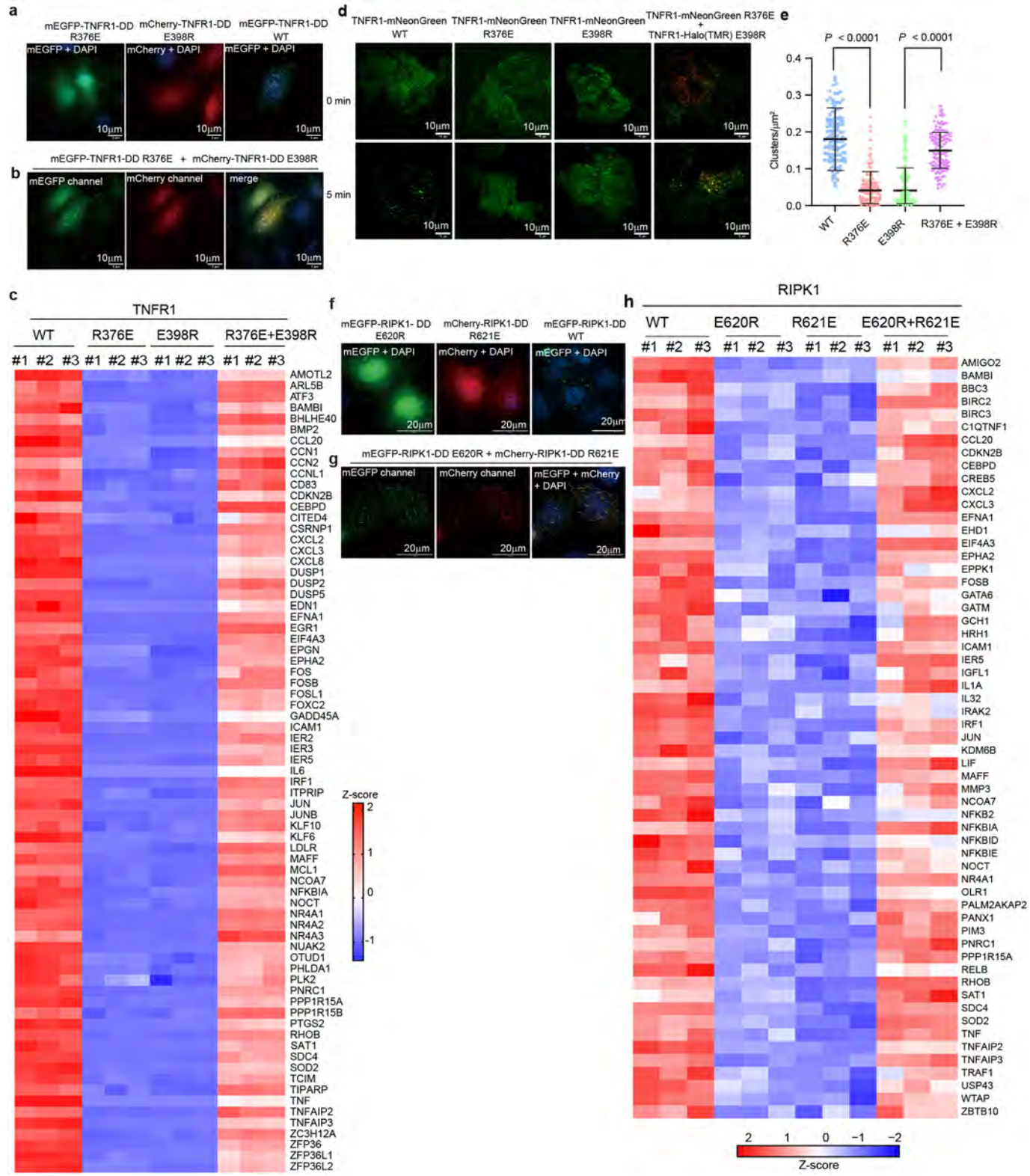
Extended Data Fig. 2 | See next page for caption.

Extended Data Fig. 2 | Cryo-EM structure determination of TNFR1-DD, TRADD-DD and RIPK1-DD ternary super complex. a, Flow chart for the first attempt of cryo-EM structure determination of co-expressed TNFR1-DD/TRADD-DD/RIPK1-DD ternary complex, which failed to yield high resolution density map. **b**, Flow charts for the purification of co-expressed TNFR1-DD/TRADD-DD/RIPK1-DD complexes without and with K596E RIPK1-DD treatment. **c-d**, Size-exclusion chromatographs and SDS-PAGE analysis of complexes purified as in b. **e**, Size-exclusion chromatographs of GB1-tagged WT RIPK1-DD and K596E RIPK1-DD protein, whose molecular weight was determined by size-exclusion chromatography coupled with multi-angle static light scattering. **f**, Distribution of the length of filaments of TNFR1-DD/TRADD-DD/RIPK1-DD complexes purified as procedure in b. Data are presented as mean ± SEM for 100 filaments in each group. **g**, Flow chart for the cryo-EM structure determination of co-expressed TNFR1-DD/TRADD-DD/RIPK1-DD ternary complex treated with K596E RIPK1-DD. **h**, The FSC curve calculated between two half maps of the refined final density volume. Results are representative of three independent experiments for (**c**-**f**). The *P*-value in **f** is derived from a two-tailed Welch's t test for comparison between two groups and presented as * ($P < 0.05$), ** ($P < 0.01$), *** ($P < 0.001$), **** ($P < 0.0001$).



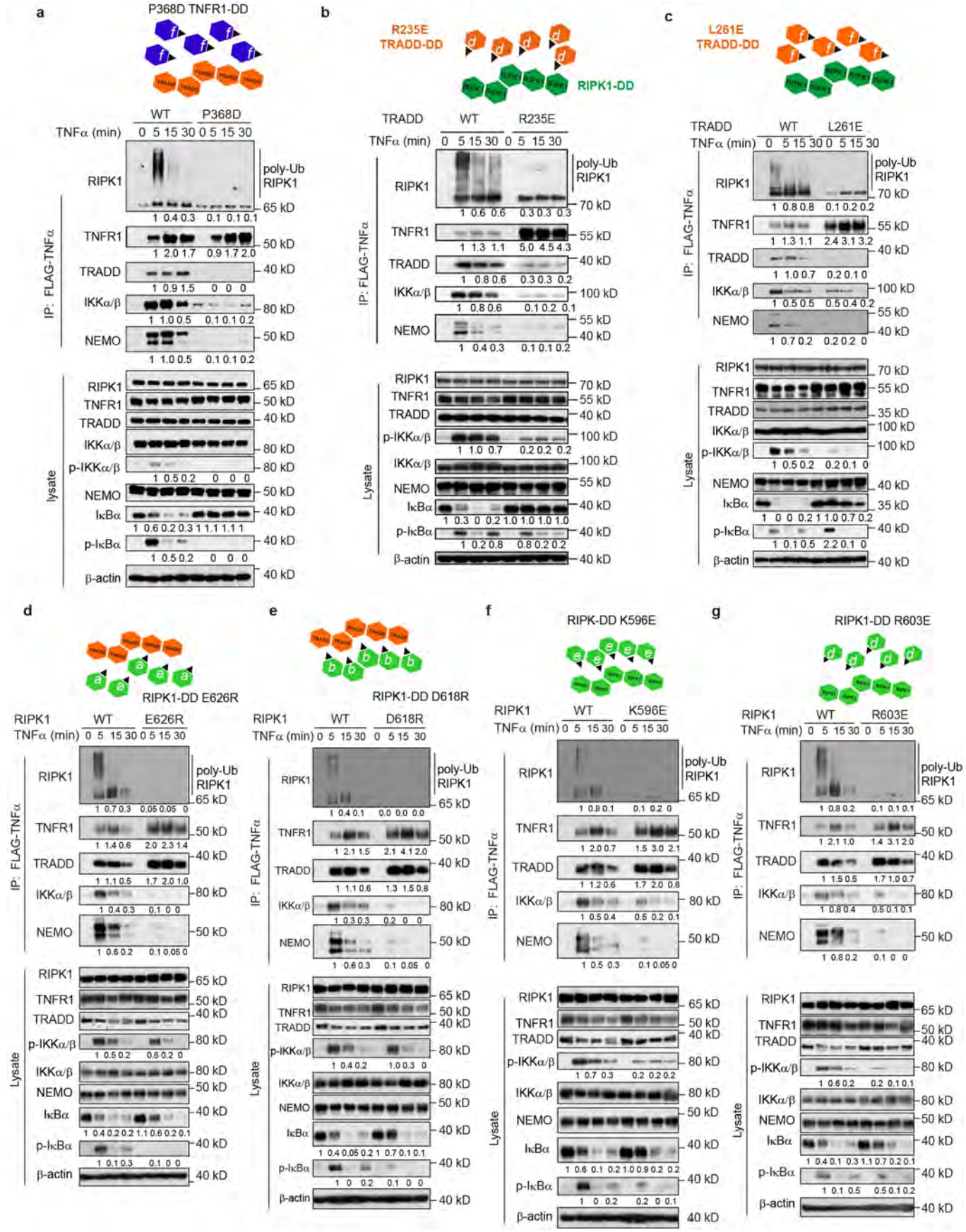
Extended Data Fig. 3 | See next page for caption.

Extended Data Fig. 3 | Structural basis for the unique assembly of TNFR1-DD/TRADD-DD/RIPK1-DD ternary complex. a-e, Cartoon representation of the association between interfaces *a* and *d* of TNFR1-DD, TRADD-DD and RIPK1-DD, with interacting residues shown as sticks and interface *a* shown as electrostatic potential surface. **f-j**, Cartoon representation of the association between interfaces *b* and *e* among TNFR1-DD, TRADD-DD and RIPK1-DD, with interacting residues shown as sticks and interface *b* shown as electrostatic potential surface. **k-o**, Cartoon representation of the association between interfaces *c* and *f* among TNFR1-DD, TRADD-DD and RIPK1-DD, with interacting residues shown as sticks and interface *c* shown as electrostatic potential surface. **p**, Energetically favourable and unfavorable assembly pathways derived based on the calculated Gibbs free energy changes (ΔG) of pairwise interactions among TNFR1-DD, TRADD-DD and RIPK1-DD pentamer layers.



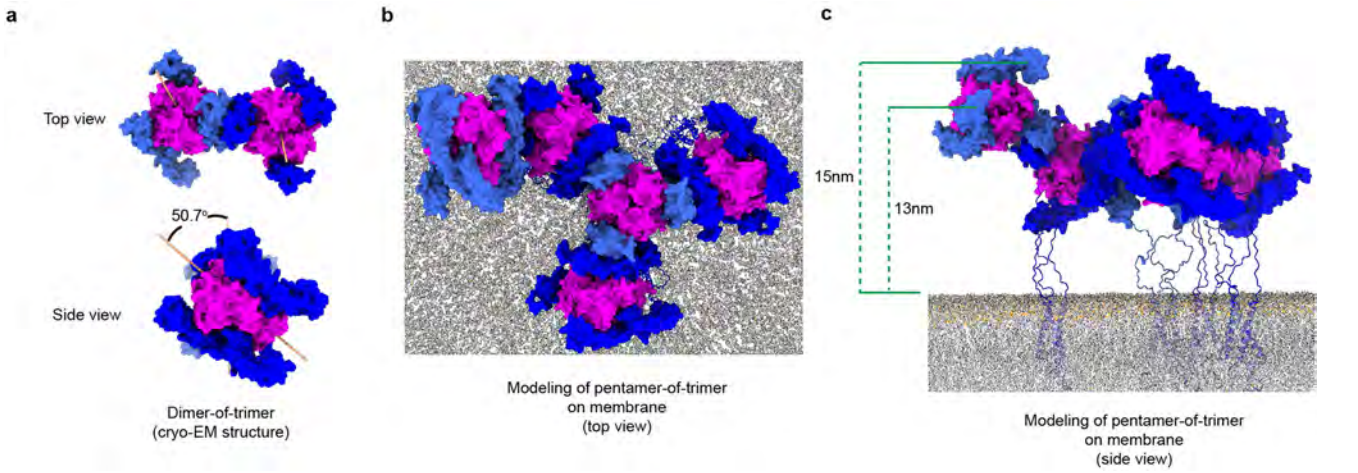
Extended Data Fig. 4 | See next page for caption.

Extended Data Fig. 4 | Both inter-layer and intra-layer DD association are critical for Complex I formation and signalling, part A. a, Fluorescence imaging of TNFR1-KO HeLa cells with individual expression of R376E and E398R TNFR1-DD mutants fused with mEGFP and mCherry tag, respectively. **b**, Fluorescence imaging of TNFR1-KO HeLa cells with co-expression of the R376E and E398R mutants in (**a**). **c**, Heatmap analysis of RNAseq of the expression level of genes induced by TNFα stimulation (100 ng/mL) for 60 min in TNFR1-KO HeLa cells reconstituted with either individual expression of WT, R376E, and E398R TNFR1 or co-expression of R376E and E398R TNFR1 mutants. **d**, TIRF imaging of individual or co-expression of full-length R376E and E398R TNFR1 mutants fused with fluorescence tag in TNFR1-KO HeLa cells after 5 min of TNFα stimulation (20 ng/mL). mNeonGreen and Halo (TMR) channels are shown in green and red, respectively. **e**, Quantitation of the puncta density on cell membranes formed by fluorescence-tagged TNFR1 variants in TNFR1-KO HeLa cells in (**d**). Data are presented as mean ± SEM for 100 areas in each group. **f**, Fluorescence imaging of RIPK1-KO HeLa cells reconstituted with individual expression of E620R and R621E RIPK1-DD mutants fused with mEGFP and mCherry tag, respectively. **g**, Fluorescence imaging of RIPK1-KO HeLa cells reconstituted by co-expression of the E620R and R621E RIPK1-DD mutants in (**f**). **h**, Heatmap analysis of RNAseq of the expression levels of genes induced by TNFα (100 ng/mL) for 60 min in RIPK1-KO HeLa cells reconstituted with WT or indicated RIPK1 variants. Results are representative of three independent experiments (**a, b, d-g**) or of three biological replicates (**c & h**). The *P*-value in (**e**) is derived from a two-tailed Welch's *t* test for comparison between two groups.

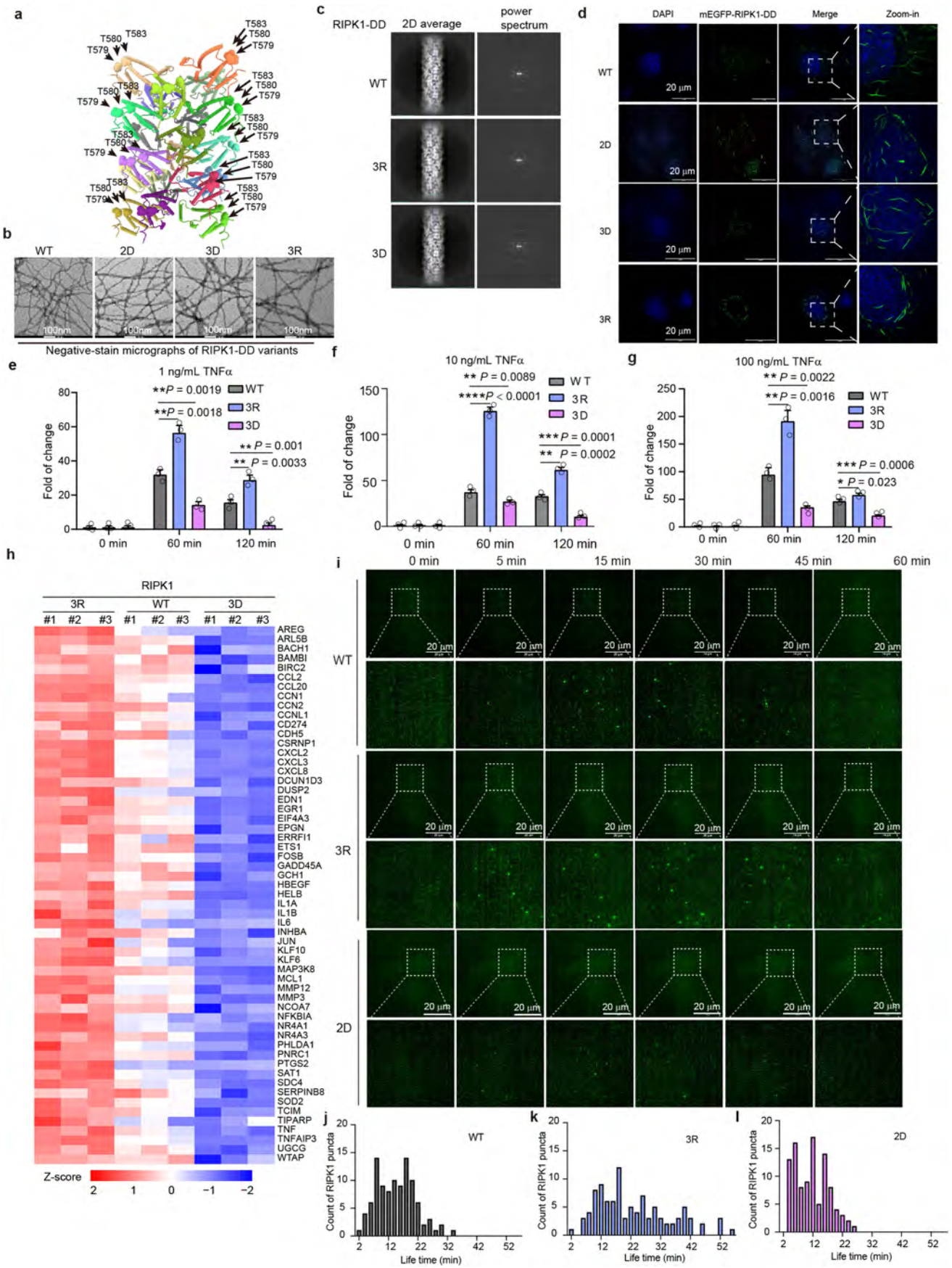


Extended Data Fig. 5 | See next page for caption.

Extended Data Fig. 5 | Both inter-layer and intra-layer DD association are critical for Complex I formation and signalling, part B. a-g, Western blotting analysis of TNFα (100 ng/mL) induced Complex I and NF-κB activation in TNFR1-KO, TRADD-KO or RIPK1-KO HeLa cells reconstituted with indicated mutants of TNFR1, TRADD and RIPK1. The relative levels of the indicated proteins normalized to β-actin are shown below blots (**a-g**). Results are representative of three independent experiments (**a-g**).

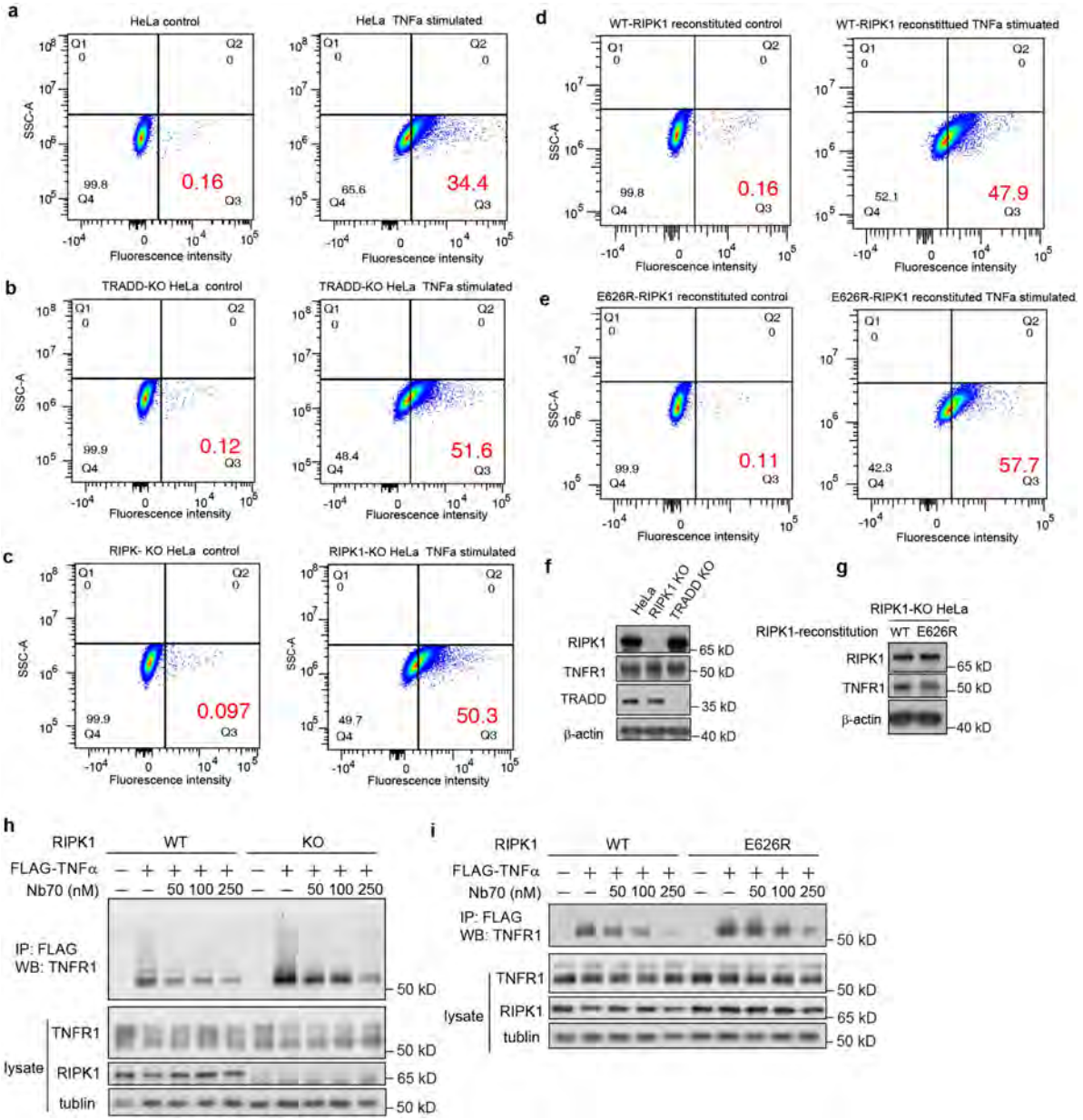


Extended Data Fig. 6 | Modelling of high-order TNFR1/TNFα clustering suggests that the ECD-TMD linker length is barely long enough for a tetramer-of-trimer cluster or 12 TNFR1s. a, Tilt of ~51° between two trimers of TNFα/TNFR1 complex in the cryo-EM structure (PDB entry 8ZUI) shown with 3-fold axis of each TNFα/TNFR1 trimer (yellow stick). **b-c**, Modelling of 5 interacting trimers of TNFα/TNFR1 complex on a flat membrane shows that the distance between ECD and TMD in the most peripheral TNFR1 exceeds the length of ECD-TMD linker. Note: The intracellular linker (~120 residues) between the TNFR1 TMD and DD is long enough to support more than 12 TNFR1 DDs that can be added to the TNFR1-TRADD-RIPK1 ternary complex. However, the extracellular linker between the ECD and TMD is only ~10 nm long (aa 184-211, 28 residues). Modelling based on the cryo-EM structure of the tetramer-of-trimer TNFR1/TNFα indicates that expanding the multimer-of-trimer interactions beyond tetramer-of-trimer would result in TNFR1-ECD of the most peripheral trimer rotating away from the TMD by at least 13 nm, which cannot be accommodated by the ECD-TMD linker unless the membrane is severely deformed.

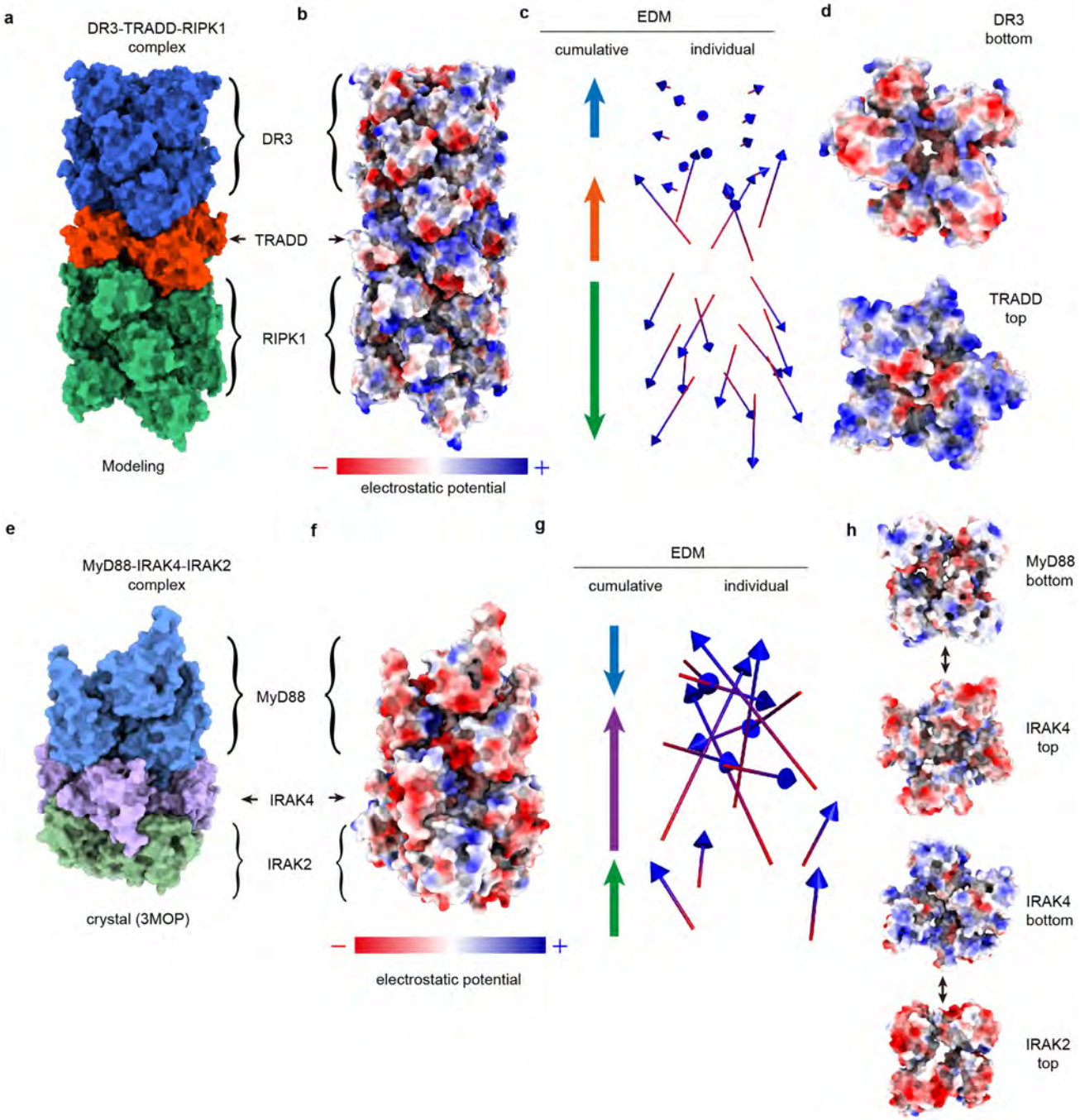


Extended Data Fig. 7 | See next page for caption.

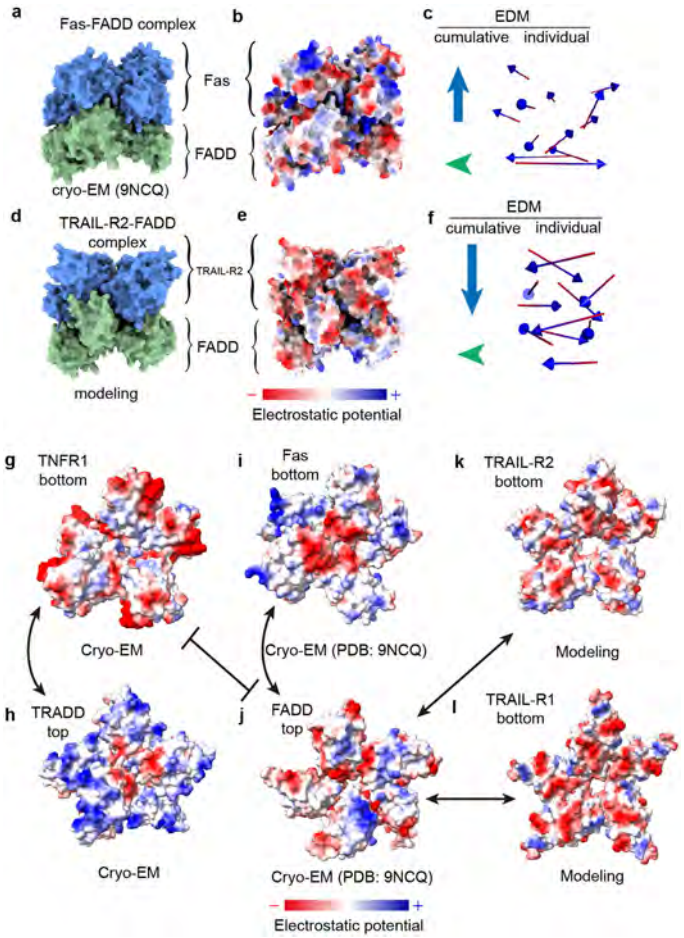
Extended Data Fig. 7 | Electric dipole moment modulates the dynamics of Complex I. a, Three sites (T579, T580 and T583, shown as spheres) on the periphery of RIPK1-DD helical oligomer are selected for mutation to change the EDM of RIPK1-DD without affecting DD-DD interactions. **b**, Negative-stain EM micrographs of fibres formed in vitro by WT, 2D, 3D or 3 R mutant RIPK1-DD purified from *E. coli*. **c**, Representative 2D images of aligned and averaged DD fibres and their Fourier-transformed power spectrum. **d**, Fluorescence imaging of fibres formed by mEGFP-tagged WT, 2D, 3D or 3 R mutant RIPK1-DD in RIPK1-KO HeLa cells. **e-g**, Quantification of A20 mRNA level by qRT-PCR in RIPK1-KO HeLa cells reconstituted with WT, 3 R or 3D RIPK1 variants induced by 1 ng/mL (**e**), 10 ng/mL (**f**) or 100 ng/mL (**g**) TNFα for 60 min. Data are presented as mean ± SEM for three biological replicates in each group. **h**, Heatmap analysis of RNAseq of the expression levels of genes induced by TNFα (10 ng/mL) for 60 min in RIPK1-KO HeLa cells reconstituted with WT, 3 R or 3D RIPK1 variants. **i**, Snap-shots of TIRF live imaging of RIPK1-KO HeLa cells expressing WT, 3 R and 2D RIPK1 tagged with mNeonGreen upon TNFα stimulation (100 ng/mL). **j-l**, Distribution of life-time of RIPK1 puncta induced by TNFα in RIPK1-KO HeLa cells expressing WT, 3 R or 2D RIPK1. Data are plotted for 100 puncta in each group. Results are representative of three independent experiments (**b, d-g & i**) or of three biological replicates (**h**). The *P*-value in (**e**-**g**) is derived from a two-tailed Welch's t test for comparison between two groups and presented as * ($P < 0.05$), ** ($P < 0.01$), *** ($P < 0.001$), **** ($P < 0.0001$).



Extended Data Fig. 8 | Intracellular Complex I assembly restricts extracellular TNFα engagement. a-c, Fluorescence-activated cell sorting (FACS) of AlexaFlour-647 labelled TNFα stimulated wildtype, TRADD-KO and RIPK1-KO HeLa cells. The Q3 fraction represents the TNFα-bound cells. **d-e**, FACS sorting of AlexaFlour-647 labelled TNFα stimulated RIPK1-KO HeLa cells reconstituted with wildtype or E626R-RIPK1. **f-g**, Western-blot showing the expression level of TNFR1, TRADD and RIPK1 in these cells. **h-i**, Co-immunoprecipitation of TNFR1 with FLAG-TNFα in the presence of nanobody Nb70 that competes with TNFα for binding to TNFR1. Results are representative of three independent experiments (**a-i**).



Extended Data Fig. 9 | Structural modelling and electric dipole moment calculation of DR3-TRADD-RIPK1 and MyD88-IRAK4-IRAK2 DD complexes. **a**, Modelling of DR3-TRADD-RIPK1 ternary DD complex based on DR3-DD alignment with TNFR1-DD in our cryo-EM structure of the TNFR1-TRADD-RIPK1 DD complex. **b-c**, Electrostatic potential surface and calculated EDMs of the DR3-TRADD-RIPK1 ternary DD complex. **d**, The electrostatic potential of the "bottom" face of the DR3-DD pentamer is complementary to the "top" face of the TRADD-DD pentamer. **e-f**, Cystal structure of the MyD88-IRAK4-IRAK2 complex (PDB ID: 3MOP) and its electrostatic potential surface. **g**, Calculated EDMs of the MyD88-IRAK4-IRAK2 complex. **h**, Electrostatic potential of DD layers in MyD88-IRAK4-IRAK2 shows charge complementation.



Extended Data Fig. 10 | Structural analysis shows the basis for the specificity of DD adaptors for different receptors. a-b, Cryo-EM structure of Fas-FADD complex and its electrostatic potential surface. **c**, Calculated EDMs of the Fas-FADD complex. **d-e**, Structural modelling of TRAIL-R2-FADD complex and its electrostatic potential surface. **f**, Calculated EDMs of the TRAIL-R2-FADD complex. **g-h**, The "bottom" face of the TNFR1-DD pentamer has a negatively charged periphery, which complements the "top" face of the TRADD-DD pentamer. **i-j**, In the Fas-DD/FADD-DD complex, the "bottom" face of the Fas-DD pentamer shows charge complementation with the "top" face of the FADD-DD pentamer, which is incompatible with the "top" face of the TRADD-DD pentamer. **k-l**, Structural modelling of the DD pentamer DD from TRAIL-R2 or TRAIL-R1. The "bottom" faces of both receptors are compatible with the "top" face of the FADD-DD pentamer, but incompatible with TRADD-DD.

Extended Data Table 1 | Statistics for cryo-EM data collection, processing, structure refinement and validation

	RIPK1-DD filament	TNFR1-DD filament	TRADD-DD filament	TNFR1-DD/ TRADD-DD/ RIPK1-DD complex
Data collection and processing				
Magnification	22500	105000	81000	81000
Voltage(kV)	300	300	300	300
Electron exposure (e/Å^2)	55	55	50	50
Defocus range (μm)	-2.3 ~ -1.3	-2.2 ~ -1.2	-2.4 ~ -1.2	-2.4 ~ -1.2
Pixel size (Å)	1.06	0.83	1.055	1.055
Helical symmetry imposed				
rise (Å)	5.22	5.31	5.19	N/A
twist (degrees)	139.36	138.36	138.4	N/A
Number of initial particle images	488860	642960	233004	104838
Number of final particle images	392912	512379	203507	68501
Map resolution (Å)				
FSC threshold	0.143	0.143	0.143	0.143
Map resolution range (Å)				
	2.87-6	2.62-6	3.31-6	3.41-6
Structure refinement				
Initial model used (PDB ID)	6ac5	1ich	6ac0	6ac0, 6ac5, 1ich
Map sharpening B factor (Å^2)	-118.6	-91.2	-107	-85.3
Model composition				
Protein residues	2000	1740	4708	2966
Non-hydrogen atoms	16360	14360	38764	24321
Ligand atoms	0	0	0	0
RMSD for bond lengths (Å)	0.003	0.008	0.008	0.003
RMSD for bond angles (°)	0.497	0.738	0.847	0.631
Validation				
MolProbity score	1.23	1.42	1.59	1.56
Clash score	4.61	6.34	11.83	10.05
Poor rotamers (%)	0	0	0.1	0..002
Ramachandran plot (%)				
favored region	98.57	97.65	98.18	97.9
allowed region	1.43	2.35	1.82	2.07
outliers	0	0	0	0.03
PDB ID of structure model	9v9e	9v9c	9vgd	9vin
EMDB ID of density volume	EMD-64870	EMD-64869	EMD-65047	EMD-65094